Title
Indirect Measurements of the Composition of Ultrafine Particles in the Arctic Late-Winter

Journal
Journal of Geophysical Research: Atmospheres, 126(22)

ISSN
2169-897X

Authors
Myers, Deanna C
Lawler, Michael J
Mauldin, Roy L
et al.

Publication Date
2021-11-27

DOI
10.1029/2021jd035428

Peer reviewed

Indirect measurements of the composition of ultrafine particles in the Arctic late-winter

Deanna C. Myers[1], Michael J. Lawler[1,2], Roy L. Mauldin[3,4], Steven Sjostedt[5], Manvendra Dubey[6], Jonathan Abbatt[7], James N. Smith[1]

[1]Department of Chemistry, University of California, Irvine, CA, 92697, USA

[2]Now at Cooperative Institute for Research in Environmental Science, CU Boulder, NOAA Earth System Research Laboratories, Boulder, CO, USA

[3]Department of Chemistry, Carnegie Mellon University, Pittsburgh, PA, USA

[4]Department of Atmospheric and Oceanic Sciences, University of Colorado, Boulder, CO, 80309, USA

[5]Morgan Community College, Fort Morgan, CO, 80701, USA

[6]Los Alamos National Laboratory, Los Alamos, NM, 87545, USA

[7]Department of Chemistry, University of Toronto, Toronto, Ontario, M5S 3H6, Canada

Abstract

We present indirect measurements of size-resolved ultrafine particle composition conducted during the Ocean–Atmosphere–Sea Ice–Snowpack (OASIS) Campaign in Utqiagvik, Alaska, during March 2009. This study focuses on measurements of size-resolved particle hygroscopicity and volatility measured over two periods of the campaign. During a period that represents background conditions in this location, particle hygroscopic growth factors (HGF) at 90% relative humidity ranged from 1.45-1.51, which combined with volatility measurements suggest a mixture of ~30% ammoniated sulfates and ~70% oxidized organics. Two separate regional ultrafine particle growth events were also observed during this campaign. Event 1 coincided with elevated levels of H_2SO_4 and solar radiation. These particles were highly hygroscopic (HGF=2.1 for 35 nm particles), but were almost fully volatilized at 160 °C. The air masses associated with both events originated over the Arctic Ocean. Event 1 was influenced by the upper marine boundary layer (200-350 m AGL), while Event 2 spent more time closer to the surface (50-150 m AGL) and over open ocean leads, suggesting marine influence in growth processes. Event 2 particles were slightly less hygroscopic (HGF=1.94 for 35nm and 1.67 for 15nm particles), and similarly volatile. We hypothesize that particles formed during both events contained 60-70% hygroscopic salts by volume, with the balance for Event 1 being sulfates and oxidized organics for Event 2. These observations suggest that primary sea spray may be an important initiator of ultrafine particle formation events in the Arctic late-winter, but a variety of processes may be responsible for condensational growth.

1 Introduction

Aerosol particles in the Arctic are known to exhibit seasonal variability in their chemical and physical properties. In many high-latitude regions, winter and early spring are dominated by Arctic Haze, a phenomenon characterized by long-range transport of anthropogenic pollutants and resulting in the highest mass concentrations of particulate matter (Barrie, 1986; Rahn, 1981; Tunved et al., 2013). Accumulation mode particles dominate during this period, largely from transport of anthropogenic pollution originating from Eurasia and North America (Barrie, 1986; Frossard et al., 2011; Heintzenberg, 1982; Law & Stohl, 2007; Quinn et al., 2007; Rahn, 1981; Tunved et al., 2013). A persistent boundary layer effectively traps pollution over the Arctic, coastal Eurasia, and much of Canada until late spring, when it recedes to polar north (Barrie, 1986). Late spring and summer are less anthropogenically influenced, and thus are characterized by lower particle mass concentrations (Browse et al., 2012; Croft et al., 2016; Freud et al., 2017; Garrett et al., 2011; Ström et al., 2003; Tunved et al., 2013). During that period, marine biogenic emissions and photochemistry are key drivers of atmospheric chemistry (Dall'Osto, et al., 2018; Quinn et al., 2002; Tunved et al., 2013). The Arctic can be a cloud condensation nuclei (CCN)-limited region (Mauritsen et al., 2011). Prior measurements of CCN concentrations have shown variation depending on the region of air mass origin; generally higher concentrations of CCN are associated with air masses from mid-latitudes (Hoppel et al., 1973; Jung et al., 2018; Moore et al., 2011; G. E. Shaw, 1986), which is common in Arctic winter and spring. Lower CCN concentrations have been measured in summertime (Martin et al., 2011), mainly from air masses originating over the Arctic Ocean (Leaitch et al., 2016; Zábori et al., 2015). Increases in particle number concentrations, especially through particle formation (Abbatt et al., 2019), can contribute significantly to CCN concentrations through condensational growth, and thus impact radiative forcing (Allan et al., 2015; Kecorius et al., 2019; Leaitch et al., 2016; Mauritsen et al., 2011).

Several recent studies have shown that the formation and growth of sub-100 nm diameter ultrafine particles (UFP) occur readily in the Arctic atmosphere (Allan et al., 2015; Asmi et al., 2016; Baccarini et al., 2020; Chang et al., 2011; Collins et al., 2017; Dall'Osto et al., 2017; Dall'Osto et al., 2018; Giamarelou et al., 2016; Heintzenberg et al., 2015; Karl et al., 2013, 2012; Kecorius et al., 2019; Kolesar et al., 2017; Kupiszewski et al., 2013; Nguyen et al., 2016; Tunved et al., 2013; Willis et al., 2016; Ziemba et al., 2010). New particle formation has been shown to occur from anthropogenic emissions during this time of year, such as those from oil fields (Creamean et al., 2018; Kolesar et al., 2017). Creamean et al. (2018) used measurements of particle light scattering to identify refractory black carbon, though neither work directly measured particle chemical composition. However, few studies to date have focused on the composition of Arctic UFP and most observations have occurred during

summer. Prior spring and summer studies have attributed UFP formation events to photochemical sulfuric acid (H_2SO_4) production (Covert & Heintzenberg, 1993), with sulfate considered an important particle component (Nyeki et al., 2005; Wiedensohler et al., 1996). These employed filters and impactors for offline chemical analysis, biasing these results to larger particles that may not represent the composition of UFPs. Size-resolved nanoparticle composition of Arctic UFPs has been studied using mostly indirect measurements, with a focus on formation and growth events during late spring and summer. In the Canadian Arctic, UFP formation was observed to occur freely in the marine boundary layer, with complementary gas-phase measurements suggesting marine biogenic sources of organic and sulfur-containing gas-phase precursors (Burkart et al., 2017). Several observations of UFP formation and growth from other Arctic locations associated these phenomena with oxidized products of dimethylsufide (DMS) like methanesulfonic acid (MSA) and H_2SO_4, suggesting a marine biogenic influence (Abbatt et al., 2019; Chang et al., 2011; Dall´Osto et al., 2018; Ferek et al., 1995; Ghahremaninezhad et al., 2016; Leaitch et al., 2013; Quinn et al., 2002). Indirect measurements of summertime particle composition in Ny-Alesund, Svalbard, indicated that organic vapor condensation plays a large role in UFP formation (Kecorius et al., 2019). Organic compounds were found to contribute to the growth of newly formed UFPs in the Canadian Arctic, with a small contribution from sulfur-containing compounds (Tremblay et al., 2019). Willis et al., (2016) showed that growth of sub-20 nm particles to ~50 nm coincided with the presence of organics, trimethylamine, and MSA in particles 80 nm and larger, suggesting the particles grew by condensation of MSA and other lower-volatility organic species. Model results from Canadian Arctic observations using a paired chemical transport-microphysics model indicate that ternary nucleation from H_2SO_4, ammonia (NH_3), and water, followed by condensation from marine biogenic species and biogenically derived sulfur compounds, accounts for more than 90% of the simulated number concentration for particles larger than 20 nm (Croft et al., 2019). Other measurements performed in late-summer suggest that iodine (Allan et al., 2015; Baccarini et al., 2020) and marine nanogels are responsible for some observed UFP formation events (Dall'Osto et al., 2017; Karl et al., 2013; Leck et al., 2013; Leck & Bigg, 2010). Measurements made during 11 particle formation events aboard the Swedish icebreaker *Oden* in August and September of 2018 found that these events coincided with elevated levels of iodic acid (HIO_3) and relatively low levels of H_2SO_4 (Baccarini et al., 2020). Fragmentation of primary marine particles followed by the condensation of low-volatility vapors have been proposed to explain numerous UFP formation events observed in the high Arctic during late spring and summer (Karl et al., 2013; Lawler et al., 2021). Taken together, these results suggest gas-phase ammonia, amines, organics, oxidized sulfur species, and fragmentation of primary marine particles contribute to the formation and growth of UFPs in the late spring and early summer in this region.

Winter and early spring measurements of UFP formation events and the composition of these particles are largely missing. This is due in part to the dominant accumulation mode that biases bulk and sub-micron measurements towards larger particles. Some insights into the mechanisms of UFP formation can nonetheless be gained through such measurements. Analysis of sub-micron aerosol particle composition during particle formation events in Tiksi, Siberia, made by aerosol mass spectrometry (AMS) found that while summertime events were driven by oxidation of biogenic low-volatility gases, early spring events are likely due to oxidation of anthropogenic precursors of Arctic Haze (Asmi et al., 2016). Filter samples have shown submicron particles are largely composed of sea salt, non-sea-salt sulfates (nss sulfate), and organic species (Kirpes et al., 2018, 2019; Patterson et al., 1967; Quinn et al., 2002; Tomasi et al., 2012). Long-term measurements taken at Utqiagvik (formerly Barrow), Alaska are consistent with other measurements indicating nss sulfate is a major component of submicron wintertime aerosol, but the concentration decreased by ~60% between 1976 and 2008. Elemental analysis indicated that while source regions remained the same over this time period, emissions decreased (Quinn et al., 2009). Soot particle AMS (SP-AMS) measurements made in Greenland have linked UFP formation in February through May to MSA and molecular iodine, suggesting contributions from both biotic and abiotic sources (Dall'Osto, Geels, et al., 2018; Dalll'Osto, Simo, et al., 2018). Since most winter-time measurements to date have been performed on bulk aerosol, Arctic UFP composition is still not understood in the winter and early spring. More measurements are needed in order to understand the mechanisms by which new particles form in this important region.

We seek to address this measurement gap by reporting indirect measurements of UFP composition made during the Ocean – Atmosphere – Sea Ice – Snowpack (OASIS) Campaign in Utqiagvik, Alaska during March 2009. A period from 27 – 31 March was determined to have winds from the Arctic Ocean, with particle properties measured during this time representing background conditions. Two separate nanoparticle growth events (12 – 14 March) were observed during the campaign, where particles grew from 5 nm to ~ 20 nm in diameter. Because particle formation is one of the primary contributors to CCN budgets in this sensitive region (Abbatt et al., 2019; Croft et al., 2016; Kecorius et al., 2019), we focus on the growth events to investigate the species involved in new particle formation and condensational growth. The background period is included in this work to assess the differences in properties between the two populations. Size-resolved hygroscopicity and volatility measured during these events were analyzed to hypothesize the species involved the growth of these newly formed particles.

2 Methods

Measurements were made during the National Science Foundation (NSF) OASIS field campaign in Utqiagvik, Alaska from 5 March through 15 April 2009 by several research groups (NCAR, 2012). Complementary measurements from National Oceanic and Atmospheric Administration (NOAA), including the solar radiation measurements and calculations of air mass backward trajectories, the National Snow and Ice Data Center (NSIDC), University of Wisconsin Space and Science Engineering Center, and National Aeronautics and Space Administration (NASA) Global Modeling and Assimilation Office were also used. All times are reported in Alaska Daylight Time (AKDT; UTC – 8 hours) and are referred to as "local time" in this work.

2.1 Site description

Particle measurements were collected in a Quonset hut at the U.S. Navel Arctic Research Laboratory (NARL) and trace gas and surface meteorology measurements were performed approx. 1 km away in buildings located near the Barrow Arctic Research Center (BARC). Numerous measurements of key trace gases and particle properties, as well as of meteorology, were made over the course of the campaign; those pertinent during the time periods of interest are outlined below.

2.2 Air mass origin and station meteorology

Air mass backward trajectories were calculated to determine source influences for each of the ultrafine particle events observed using the NOAA Hybrid Single-Particle Lagrangian Integrated Trajectory (HYSPLIT) transport model (Rolph et al., 2017; Stein et al., 2015). Backward trajectories of 72-hour duration were determined for air masses arriving 50 meters above ground level (AGL) at the measurement site at the beginning and halfway through the UFP events (Event 1: 3/12/09 04:07 – 19:02 ADT; Event 2: 3/13/09 20:37 – 3/14/09 3:47 ADT) using the Global Data Assimilation System (GDAS) 1° meteorology. Satellite images from NASA Moderate Resolution Imaging Spectroradiometer (MODIS)/Aqua Sea Ice Extent from the NSIDC (MYD29 Version 6, https://nsidc.org/data/MYD29/versions/6) and Aqua corrected reflectance (true color) (MYD02QKM Version 6, https://ladsweb.modaps.eosdis.nasa.gov/archive/allData/61/MYD02QKM/) with temporal resolution of 5 minutes and spatial resolution of 1 kilometer were provided by the Earth Observation System Data Gateway and used to visually identify leads and areas of open water in the sea ice (Hall & Riggs, 2015). Images were analyzed for 9 – 14 March, corresponding to the timespan of the HYSPLIT back trajectories calculated for each UFP growth event observed. Visually identified leads were confirmed using the algorithm developed by Hoffman et al. (2019), in which Aqua (DOI: 10.5067/MODIS/MYD021KM.061) and Terra (DOI: 10.5067/MODIS/MOD021KM.061) satellite MODIS data of brightness temperature are analyzed for cloud masks to identify lead pixels, which are

then confirmed using image processing to analyze shape characteristics. Daily Arctic Sea ice leads identified through this algorithm are publicly available from University of Wisconsin Space and Science Engineering Center (https://www.ssec.wisc.edu/leads/).

Sonic anemometers (Applied Technologies, Sonic Anemometer/Thermometer model SATI/3K) were used to measure three-dimensional wind velocities at 10 Hz. Wind speed and direction were obtained from vector-averaging the horizontal wind velocities over 1-minute intervals and are accurate to ± 0.03 m s^{-1} and ± 0.1°, respectively. Wind direction data are color-coded based on area of origin relative to the measurement sites to identify periods with likely local influences at the sites (labelled "Utqiagvik", 110 - 180°; "local building", 180 – 300°; and "local NNW", 300 – 10°) and periods with minimal local influence (labelled "clean", 10 – 110°). Time periods with "calm" winds were those with minimal wind (wind speed < 1 m s^{-1}).

Measurement of solar radiation were conducted at the NOAA Earth System Research Laboratory (ESRL) Global Monitoring Division (GMD) Barrow Atmospheric Baseline Observatory (BRW), located approximately 3.5 km northeast of NARL. We report 1-minute measurements of downwelling global solar radiation (W m^{-2}), performed with an unshaded Precision Spectral Pyranometer (Eppley). Data are publicly available through the NOAA/GMD database (https://gml.noaa.gov/dv/data/).

Wind speeds over the open sea ice leads were estimated using reanalysis data obtained from NASA's Modern-Era Retrospective analysis for Research and Applications version 2 (MERRA-2) (Global Modeling and Assimilation Office (GMAO), 2015) for the time period 10 – 12 March. These data have temporal resolution of 3 hours and spatial resolution of 0.5 ° x 0.625 °.

2.3 Particle physical, chemical, and radiative properties

2.3.1 Particle number size distributions

We note that ambient atmospheric temperatures during the measurement periods generally ranged from -20 to -30 °C while the instruments described here maintained a temperature within the Quonset hut of ~14 °C, likely leading to evaporation of some volatile particulate compounds. Particle number size distributions for particles with electrical mobility diameter of 4 nm to 1 μm were collected using a particle size distribution system consisting of 3 instruments that measure with a 5-minute time resolution. A nanometer scanning mobility particle sizer (nano-SMPS) comprised of a home-built bipolar neutralizer, a TSI model 3085 Differential Mobility Analyzer (DMA), a home-built high voltage and flow control system, and an Ultrafine Condensation Particle Counter (UCPC, TSI model 3025a), covered the particle mobility range of 4 to 30 nm. A scanning mobility particle sizer (SMPS), identical to the nano-SMPS

except for the use of a TSI model 3081 DMA and a standard condensation particle counter (CPC, TSI model 7620, modified to run at 1.2 lpm aerosol flow rate), measured particles of diameter ~22 to ~225 nm. An optical particle counter (OPC, Lasair model 1003 PMS, Inc.) measured particle number-size distributions over the diameter range of 0.1 to 1 μm. Measured distributions were combined to create a continuous size distribution. In most of the cases, we find good agreement (<10% difference) between the nano-SMPS and SMPS in the overlapping diameters when the ambient size distribution was stable. During less stable conditions, we observed larger differences in the overlap region that we attribute to the 2.5 min that separated the detection of the largest diameters of the nano-SMPS and the smallest diameters of the SMPS. For this reason, we averaged the measured $dN/dlogD_p$ in this overlap region. The OPC measures optical diameter, which can vary significantly from the SMPS-measured mobility diameter due to uncertainties in the refractive index. As discussed in Hand & Kreidenweis (2002), the optical diameter for an OPC that is calibrated using polystyrene latex beads (refractive index of 1.59) is ~30% lower than the physical diameter for 0.1 μm ammonium sulfate particles and decreases to 5% at 1 μm. After confirming that our OPC performed similarly to that used in the Hand and Kreidenweis study, we applied the corrections they recommend to the optical diameter assuming that particles in this size range were primarily ammonium sulfate, which has a refractive index (1.53) similar to that of NaCl (1.55). In most cases this significantly improved overlap in this size range and resulted in reasonable agreement (<25%) during periods when the ambient size distribution was stable. After this correction, we averaged the measured $dN/dlogD_p$ in the overlap region of the SMPS and OPC.

The average particle growth rate was calculated using these data following the method outlined in Dal Maso et al. (2005), in which a linear regression was fitted to the log-normal number-weighted mode particle diameter of the growth event versus time during the growth period. Gamma (Γ; Section 3.3) was calculated using this growth rate (Kuang et al., 2010). The particle size distribution data was also used to estimate the condensation sink (CS) during particle growth events, using the method detailed in Kulmala et al. (2001). Size distributions were corrected for the transmission efficiency of the inlet tubing using a model predictions that assume laminar flow, the latter of which was confirmed by our inlet flow rate measurements (Hinds, 1999).

2.3.2 Particle optical properties

Sub-2 μm ambient particle absorption and scattering coefficients were measured simultaneously at 781 nm using a photoacoustic soot spectrometer (PASS-1, Droplet Measurement Technologies using the operational protocol described in Flowers et al. (2010). The PASS-1 measured aerosol particle absorption coefficients (β_{abs}) at 781 nm directly using the photoacoustic technique and scattering coefficients (β_{sca}) with an integrating nephelometer. Noise was removed from collected data using a

bandpass filter, with a band set between 0 and 12 M m^{-1} for scattering data, and 0 and 30 M m^{-1} for the absorption data. The instrument was zeroed every 40 minutes to eliminate systematic drifts and the reported measurements were averaged in 150 second bins to enhance signal to noise. Particle single scattering albedo (SSA) was calculated as follows:

$$SSA = \frac{\beta_{sca}}{\beta_{sca} + \beta_{abs}} \quad (1)$$

Calculated values of SSA were used to determine the relative absorbing versus scattering properties of larger aerosol particles (D_p > 110 nm) during periods of interest, and to identify periods of local pollution such as that provided by snow removal equipment that have low SSA due to absorbing soot emissions, which would not have been identified from wind direction measurements.

2.3.3 Indirect measurements of particle chemical properties

A hygroscopicity tandem differential mobility analyzer (HTDMA) measured the hygroscopic growth factor of size-selected particles at 90% relative humidity (RH). In this home-built instrument, which is also described in detail elsewhere (Lance et al., 2013), particles were neutralized with a bipolar neutralizer, dried to ~2% RH, and then size-selected by the first DMA (home-built, but identical in design to TSI model 3081). Dry particle sizes studied had electrical mobility diameters ($Dp(RH_{dry})$) of 15, 35, 50, 75, and 110 nm. Size-selected particles then passed to the conditioning chamber, where they were exposed to a controlled 90% RH generated by mixing humidified and dried air into the shell of multitube Permapure Nafion humidifiers. The resulting size distribution was measured by a second, identical DMA operated in stepping mode and a CPC (TSI model 3010). Sheath and excess flows in the DMAs were 5 lpm with an aerosol flow of 0.6 lpm. The instrument was maintained at a controlled temperature of 15 ± 2 °C using a recirculating air bath, and RH was monitored throughout the instrument with humidity sensors, which are accurate to ±3 % in the ranges used in this work. The RH in the second DMA during the periods of interest was relatively stable, averaging 89.7 ± 0.9 % during the particle growth events and 93.6 ± 2.1 % during the background period. Data was inverted using the TDMAinv algorithm developed by Gysel et al., (2009), and corrected for variations in relative humidity in the second DMA using methods outlined in Gysel et al. (2009) and Keith and Arons (1954). All corrected size distributions during the periods discussed below consisted of a single mode, suggesting internally mixed aerosol (Weingartner et al., 2001). These size distributions were fitted with a Gaussian curve and the peak of the curve was used to represent the peak diameter of the humidified mode $Dp(RH_{humid})$. Hygroscopic growth factor (*HGF*) was calculated using:

$$HGF = \frac{Dp(RH_{humid})}{Dp(RH_{dry})} \quad (2)$$

From measurements of HGF, we then estimate the volume fraction of representative particulate compounds using the Zdanovskii-Stokes-Robinson (ZSR) relation:

$$HGF_{meas} = (\sum_k \varepsilon_k HGF_k^3)^{1/3}$$

where ε_k is the volume fraction of pure component k in the particle and HGF_k is the growth factor of pure component k (Malm & Kreidenweis, 1997; Stokes & Robinson, 1966). Volume fractions were constrained by the composition inferred from the volatility measurements, similarly to Cravigan et al., (2020) and Modini et al., (2010), during both the background period and particle growth events, as well as measurements of H_2SO_4 and resulting Γ calculations during both growth events, similar to the method used by Giamarelou et al., (2016).

A volatility TDMA (VTDMA) measured the volatility of size-selected particles at different temperatures. Ambient particles were neutralized and size-selected by the first DMA (TSI model 3081) at mobility diameters of 15, 35, 75, and 110 nm. Particles then passed through a fast stepping/scanning thermodenuder built by Aerodyne Research, Inc., and modeled after the system described by Huffman et al. (2008). The thermodenuder was stepped at temperatures of T_D = 30, 40, 80, and 160 °C, and time was allowed during each step for the temperature to stabilize before measurement. The sample flow downstream of the thermodenuder was rapidly returned to room temperature using copper tubing and a fan-based heat exchanger. Our choice of a heat exchanger in place of an activated carbon (AC) denuder is based on prior studies that have shown that AC denuders are unnecessary for ambient conditions and may in fact cause some particles to continue to evaporate (Park et al., 2013; Saleh et al., 2011). The final particle number-size distribution was measured with the second DMA (TSI model 3081) and CPC (TSI model 3010). Since particles were not re-neutralized before the second DMA, it's possible that larger particles with two or more charges could bias the results of the volatility distributions presented here (Oxford et al., 2020). This effect is insignificant for 15 and 35 nm mobility-selected particles, since the concentration of doubly charged particles is ~0% and <1% that of singly charged positive particles (Wiedensohler, 1988). For 75 and 110 nm mobility-selected particles, this ratio is 9% and 17%, respectively. Thus this effect, if it were to bias the data, may potentially apply to these samples at levels that are suggested by the estimated charge fractions. The sample flow rate through the denuder was set to 0.6 LPM, which was determined to be optimal for this design by Wehner et al. (2002). Like the HTDMA, sheath flows in the DMAs were 5 lpm with a particle flow of 0.6 lpm. Number-size distribution data was inverted using the TDMAinv algorithm (Gysel et al., 2009). Data are reported at each temperature as the volume fraction remaining, *VFR*, which is defined as:

$$VFR = \frac{V_T}{V_{30°C}} \quad (3)$$

where V_T is the integrated total particulate volume (assuming spherical particles) at temperature, *T*. Since, as mentioned previously, the temperature inside the Quonset hut was significantly lower than ambient air, and because the Quonset hut temperature was poorly controlled, we chose to divide V_T by the integrated volume of particles exposed to our lowest controlled temperature, 30 °C ($V_{30°C}$), in our calculations of *VFR*. Estimations of particle volume fraction made using the ZSR relation were constrained by *VFR* calculations. Prior to analysis, some instrument noise was easily identified in data as repetitive modes present throughout the sampling and calibration periods and was consequently removed.

Both the HTDMA and VTDMA were calibrated at the site, before and after the observation period, using known particle standard aerosol that was aerosolized using a commercial aerosol generator (TSI model 3076). The HTDMA system was calibrated with ammonium sulfate, where measured *HGF* was found to be in good agreement with literature values (Biskos et al., 2006; Hämeri et al., 2000; Sakurai et al., 2005). Temperature in the thermodenuder was stable at each setpoint; all measurements reported were collected at temperatures within 2.5 % of the setpoint temperature. The VTDMA performance was assessed with sodium chloride and ammonium sulfate, and the data was consistent with prior volatility studies (Burtscher et al., 2001; Jennings & O'Dowd, 1990). These experiments confirmed that both instruments were operating properly and that no further adjustments to the data, other than those described above, were needed.

2.4 Trace Gas Analysis

Gas-phase concentration measurements of H_2SO_4, OH, and MSA were obtained using a selected ion chemical ionization mass spectrometer (SICIMS). Measurements were made using an inlet ~ 1.5 m above the snow surface in a building located ~ 500 m east of the particle measurement location. Details of this instrument have been previously reported in Tanner et al., (1997) and Mauldin et al., (1998). Data were calibrated following procedures outlined in Eisele & Tanner, (1991, 1993. Briefly, OH is generated from photolysis of a known amount of ozone using a well-characterized laser in a known mixture of water and nitrogen, and then titrated with a known concentration of sulfur dioxide to generate H_2SO_4; the ratio of bisulfate to nitrate ions is measured to calibrate the instrument signal. Data are presented as 30-second averages.

3 Results and Discussion

3.1 Campaign overview

The foci of the OASIS campaign were on gas-phase exchanges between the ocean, atmosphere, sea ice, and snowpack, the impact of these processes on oxidation capacity in the remote Arctic atmosphere, and how they may change with a changing climate (NCAR, 2012). The measurement period during late winter and early spring is chemically interesting because of the appearance of light at the end of polar winter (Barrie, 1986). With increasing solar radiation during the course of this campaign, photochemistry became progressively more important during the observation period (Fig. 1). Several major findings from OASIS have thus far related to gas-phase photochemical halogen chemistry, with a particular focus on bromine, including its efficacy in ozone (O_3) depletion compared to chlorine (Thompson et al., 2015) and its recycling process (Frieß et al., 2011; Liao et al., 2012). This work presents the first analysis of the complementary particle-phase measurements made during this period.

Throughout the course of the campaign, there are two prominent features in the particle size distribution measurements: sub-20 nm particles appear at the site at an initial diameter of 5 nm in bursts, with no *in situ* nucleation observed at the site as evidenced by the lack of sub-5 nm diameter particles (campaign average with 95 % confidence interval 1.4 ± 0.2 cm^{-3} in this size range); and a continuous mode centered at 200 nm (Figure 1). Average particle number concentrations, reported with a 95 %

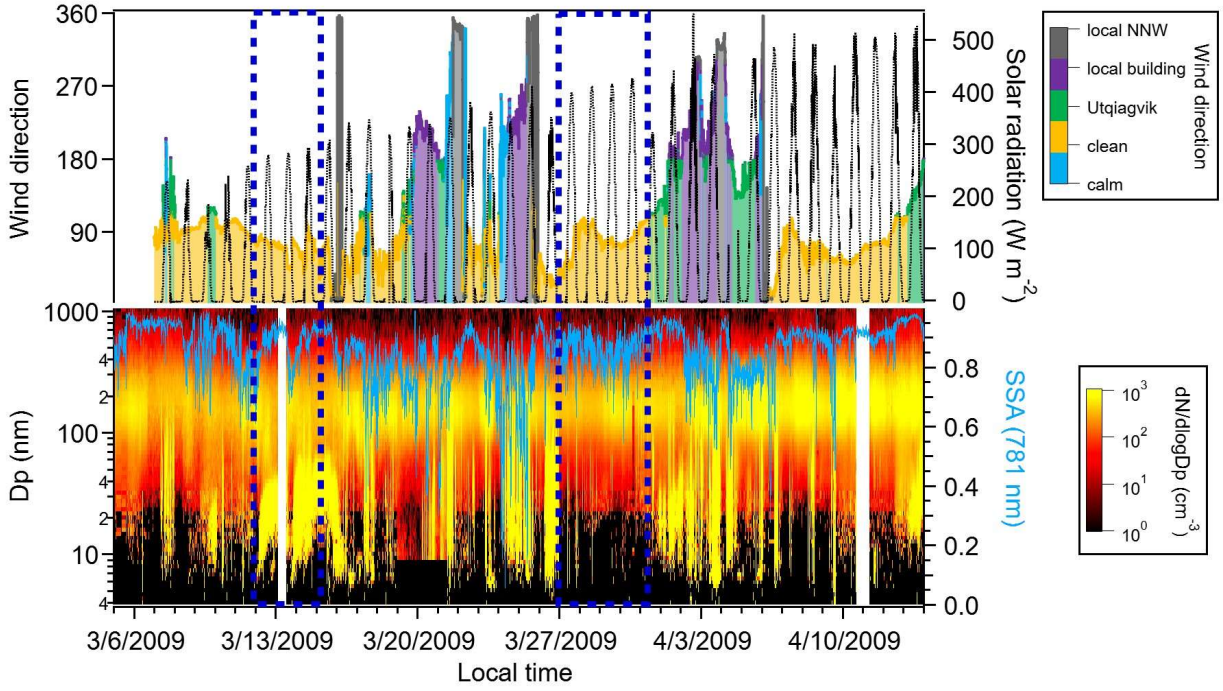

Figure 1. Meteorological data and bulk particle properties during the entire OASIS observation period. Plotted above are wind direction (color-coded to show relative direction of origin) and downwelling solar radiation. The lower plot is the particle number size distribution (diameters 4 to 1000 nm) and single scattering albedo measured at 781 nm (light blue). The focus of this work is a background period (27 – 31 March) and two distinct ultrafine particle growth events (12 – 14 March), which are boxed in blue.

confidence interval, were generally lower when the wind direction was "clean" (1040 ± 90 cm^{-3}) compared to "local building" (2270 ± 360 cm^{-3}), "local NNW" (2900 ± 830 cm^{-3}), "Utqiagvik" (2700 ± 358 cm^{-3}), and "calm" (2950 ± 600 cm^{-3}). Large variability in these average concentrations was observed between all wind directions. Note that the campaign-averaged value of SSA for all wind directions is ~0.8, with decreases to values of ~0.5 during periods with "local building" and "local NNW" influence (Figure 1). Shantz et al., (2014) reported values from 0.88 – 0.97 for SSA at 700 nm during flights made in April 2008 above Fairbanks and Utqiagvik, Alaska using a similar instrument and particle size range, which is consistent with prior Arctic measurements of SSA (Clarke et al., 1984; Delene & Ogren, 2002). This indicates that local particle emissions are more highly absorbing than ambient Arctic particles in this region, which has been observed in numerous Arctic sites during this time of year (Bodhaine et al., 1981; Clarke et al., 1984; Patterson et al., 1967; Polissar et al., 2001; Tomasi et al., 2012).

3.2 Background period

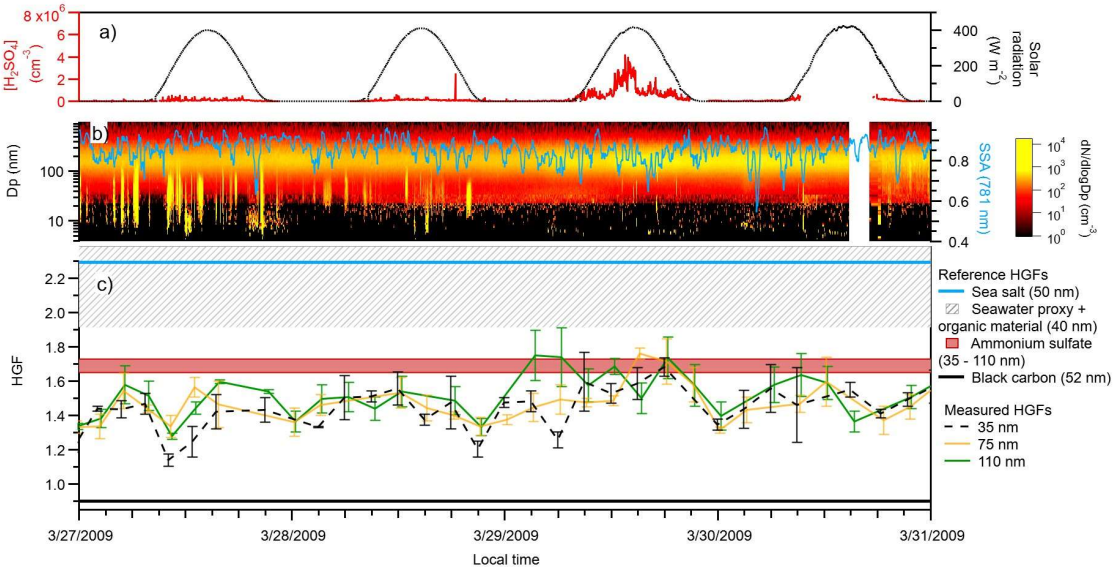

Figure 2. Particle properties measured during the background period, showing (a) H_2SO_4 concentration (red), downwelling solar radiation (black); (b) particle size distribution for particle sizes between 4 and 1000 nm in diameter, and single scattering albedo (light blue); and (c) measured particle growth factors for 35 nm (black, dashed), 75 nm (gold), and 110 nm (green, dashed) particles. Also plotted are reference growth factors for sea salt (light blue; Zieger et al., 2017), seawater proxy with organic material (gray hashed; Fuentes et al., 2011), ammonium sulfate (red, 35 – 110 nm size selected; Hämeri et al., 2000), and black carbon (black, Weingartner et al., 1995).

We begin by reporting measurements made during a period (27 – 31 March) that we identified as "clean", based on wind direction, in order to explore regional Arctic UFP physicochemical properties and address the lack of winter and spring observations. Figure 2 shows a summary of the data that include, to the best of our knowledge, the first indirect chemical composition measurements of size-selected, sub-500

nm atmospheric particles in the Utqiagvik area. While prior studies in this location have used light extinction to draw conclusions about aerosol sources (Quinn et al., 2002; P. M. Shaw et al., 2010), the measurements we present here provide a more detailed estimate of the fractional contribution of all particle constituents. Bulk particle SSA was, on average, 0.861 ± 0.055, indicating substantially more light scattering than absorbing and thus internally mixed black carbon (BC) in this region (Chen et al., 2014; Flowers et al., 2010; Liu et al., 2015), and showed relatively low variability, suggesting that local emissions did not substantially bias our measurements during this period. Like the rest of the campaign, sub-20 nm particle concentrations were very low, averaging 60 cm^{-3}, while the total number concentration during the period averaged 380 cm^{-3}. In comparison to other Arctic measurements made in March, this is lower than the concentration measured in Siberia (Asmi et al., 2016), but about twice as high as that observed in Svalbard (Tunved et al., 2013) and Greenland (Nguyen et al., 2016). These differences in particle concentration exemplify the variability in particle properties throughout different Arctic locations.

Figure 2c shows *HGF* measured at 90% RH for 35, 75, and 110 nm size-selected ambient particles. Data for 15 nm particles are missing for both HTDMA and VTDMA instruments due to the extremely low concentrations of these particles. The figure also includes published *HGF* data for laboratory-generated sea salt particles (D_p = 50 nm) (Zieger et al., 2017), ammonium sulfate (Asmi et al., 2010; Hämeri et al., 2000; Sjogren et al., 2007), black carbon (Weingartner et al., 1995), and a seawater proxy containing varying amounts of organic material on the order of those measured in surface waters in the Atlantic and Pacific Oceans during algal blooms (D_p = 40 nm) (Fuentes et al., 2011), the latter a phenomenon recently observed during Arctic winter and spring (Assmy et al., 2017; Hancke et al., 2018; Randelhoff et al., 2020). For the duration of the background period, ambient particles were less hygroscopic than sea salt and seawater proxy references, with average *HGF*s of 1.42 ± 0.13 (D_p = 35 nm), 1.52 ± 0.11 (D_p = 75 nm), and 1.49 ± 0.12 (D_p = 110 nm) measured. There is no evidence of size-dependence on *HGF* during this period since the values and their respective standard deviations all lie within the same range.

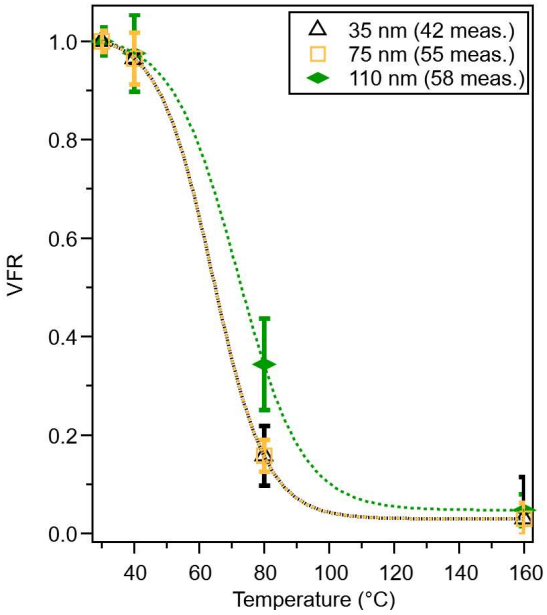

Figure 3. Average volume fraction remaining at 40, 80, and 160 °C for 35, 75 and 110 nm size-selected particles during the background period (27 – 31 March) with sigmoidal fits to data. The error bars represent standard deviation and the number of measurements at each size is shown in the legend. Initial volume (*VFR* =1) is assumed to be the volume at 30 °C.

Figure 3 shows the *VFR* for ambient 35, 75 and 110 nm size-selected particles. Negligible particle volume is lost at all sizes upon heating to 40 °C (3.52 ± 0.011 %, 3.53 ± 0.20 % and 2.54 ± 0.78 %, respectively), which corresponds to the loss of higher-volatility compounds such as semivolatile organics (Burtscher et al., 2001; Häkkinen et al., 2012; Kreidenweis et al., 1998). Volume loss at 80 °C, indicative of evaporation of lower-volatility organic species (Burtscher et al., 2001; Häkkinen et al., 2012; Kreidenweis et al., 1998) and certain higher volatility inorganic salts (Bergin et al., 1997), accounts for 80.8 ± 0.2% of the volume for sampled 35 nm particles, 84.3 ± 0.2 % of the volume for sampled 75 nm particles and 65.7 ± 0.9 % of the volume for 110 nm sampled particles. Nearly all particle volume was lost upon heating to 160 °C; at this temperature, 3.0 ± 0.1 % of the total volume of 35 nm size-selected particles, 2.9 ± 0.2 % of the total volume of 75 nm size-selected particles and 4.7 ± 2.3 % of the total volume of 110 nm size-selected particles remained. This likely is BC and may explain the average SSA values measured during this time period, which indicate that BC is internally mixed in bulk aerosol.

Combining the results of the *HGF* and *VFR* analyses provides insights into the composition of background UFPs. The high-volume loss of particles at 80 °C makes it unlikely that a significant fraction of UFP volume consists of low-volatility inorganic salts. This is supported by the *HGF* analysis that shows significantly lower hygroscopicity compared to sea salt and seawater proxy reference particles (Figure 2c). The observed evaporation behavior is consistent with sulfate that is partially or fully neutralized by a base such as ammonia, which is expected to fully evaporate at temperatures below 160 °C as confirmed by our calibrations as well as those performed by Huffman et al., (2008) using a similar instrument. The measured *HGF* is slightly below than that of ammonium sulfate (Figure 2c) with the exception of a period of elevated gas phase H_2SO_4 on 29 March during which *HGF* increased slightly, supporting a contribution of sulfate to UFP composition with the addition of a less hygroscopic material. This leads us to hypothesize that UFPs also contain some fraction of lower hygroscopicity organics. Organic compounds are routinely detected in marine aerosol (Cochran et al., 2017; O'Dowd et al., 2004; Prather et al., 2013). A mixture of organics and sulfate is also consistent with the measured *VFR* data, as loss of particulate volume over the size range of 40 – 160 °C is consistent not only with ammonium sulfate but with oxidized organics (Huffman et al., 2009). Our measurements suggest that, while it may be possible that primary organics contribute to background UFP composition, the observation that *VFR* is nearly zero at 160 °C suggests minimal contribution from low-volatility primary marine organic species (Frossard et al., 2014), and a small contribution from black carbon (Jennings et al., 1994). The measured *HGFs* may be consistent with that measured for marine nanogels (Hawkins & Russell, 2010; Ovadnevaite et al., 2011), the latter of which ranged from 1.2 to 1.3 at 90% RH. The behavior of aerosolized marine nanogels has not been well-characterized, though several prior studies have suggested that volume changes may occur in the temperature ranges studied here (Verdugo, 2012; Verdugo & Santschi, 2010).

An estimate of the volume fractions of sulfate salt and organic species, using the *HGFs* of ammonium sulfate (1.7) (Hämeri et al., 2000) and atmospheric organic matter (1.2) (Gysel et al., 2004), was performed using the average ambient *HGF* measured for each particle size reported above. Using the ZSR method with these assumptions, we estimate that, on average, volume fractions of ammonium sulfate (ε_{AS}) and organic species (ε_{ORG}) were 0.48 and 0.52 for 35 nm particles, 0.44 and 0.56 for 75 nm particles, and 0.50 and 0.50 for 110 nm particles, respectively. Estimations of volume fraction using H_2SO_4 as a third component (*HGF* = 1.9, ε_{SA}) were more consistent with the *VFR* measured for the larger particle sizes; for 35 nm, $\varepsilon_{AS} = 0.10$, $\varepsilon_{SA} = 0.20$, $\varepsilon_{ORG} = 0.70$; for 75 nm, $\varepsilon_{AS} = 0.10$, $\varepsilon_{SA} = 0.23$, $\varepsilon_{ORG} = 0.67$; and for 110 nm, $\varepsilon_{AS} = 0.10$, $\varepsilon_{SA} = 0.27$, $\varepsilon_{ORG} = 0.63$. These estimates support the hypothesis that partially neutralized sulfate and organic species contribute mainly to the observed UFP volume under background conditions.

3.3 Ultrafine particle growth events

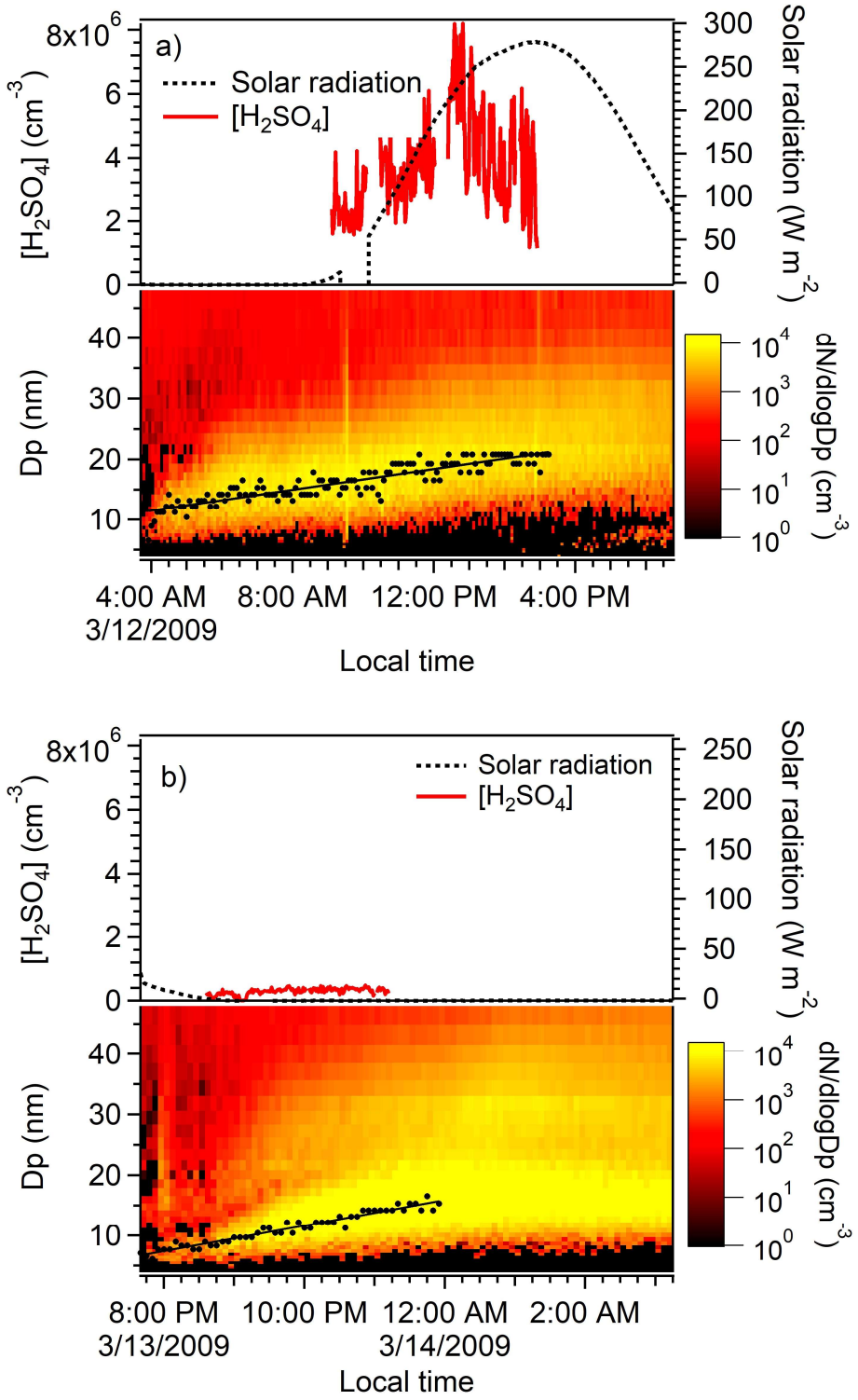

Figure 4. Photochemical and particle size distribution properties during ultrafine particle growth (a) Event 1 and (b) Event 2. Plotted are the gas-phase concentrations of H_2SO_4 (red, molecules cm^{-3}) and downwelling solar radiation (black dashes, W m^{-2}). Particle number size distributions for each growth event are shown with the mode diameter during the growth period and its linear regression fit to determine growth rates are shown in black.

In mid-March there were two distinct UFP growth events observed at the site occurring on

consecutive days (Figure 4). Both occurred during a "clean" period and there was no evidence in SSA data (Event 1: 0.85 ± 0.08; Event 2: 0.86 ± 0.03) to suggest any site-specific pollution impacting the particle properties measured. Bulk particle SSA measured during both periods were very similar to both each other and the background period average. Event 1 was first observed at the site at just after 4:00 local time on 12 March, with particles appearing at a modal diameter of 11 nm. The modal diameter increased linearly over a 12-hour period to 21 nm, corresponding to a growth rate 0.9 ± 0.1 nm h^{-1}. The CS for particles larger than those in the growing mode (D_p > 30 nm) increased from 4.8 x 10^{-3} s^{-1} to 5.6 x 10^{-3} s^{-1} over the duration of the growth, with an average of 5.1 x 10^{-3} s^{-1}. This event coincided with solar radiation at the site and an average measured H_2SO_4 concentration of 3.7 x 10^6 molecules cm^{-3}. Event 2 was first observed at the site on 13 March at 20:40, with a measured modal diameter of 7 nm. Growth lasted for ~4 hours and ended at 15 nm, with a measured modal growth rate of 2.1 ± 0.1 nm h^{-1}. This mode persisted after midnight, but no longer displayed growth (growth rate reached zero), though a separate, larger growing mode appeared. Growth was determined to end when the mode diameter remained constant for 1 hour, though we note that the bursts of particles in both events persist for longer than the growth period. The CS during the growth period for particles larger than 25 nm in diameter increased from 3.9 x 10^{-3} s^{-1} to 7.5 x 10^{-3}, with an average 6.5 x 10^{-3} s^{-1}. The event occurred at nighttime, thus solar radiation was minimal and the average concentration of H_2SO_4 was 3.0 x 10^5 molecules cm^{-3}, which is close to the SICIMS lower limit of detection. CS measured during Event 1 is consistent with previous measurements made just before particle growth events observed in March in Utqiagvik (Kolesar et al., 2017), while that for Event 2 is consistent with the larger values of CS measured during the summer in Ny-Alesund, Svalbard (Giamarelou et al., 2016). We hypothesize that the observed growth in both events ended because of the increases in CS for larger particles, meaning there was less condensable vapors to contribute to the growth of these new particles (Kulmala et al., 2001), as well as likely air mass changes, as indicated by the changes in wind direction corresponding to the end of the burst of particles (Fig. 1) (Kivekäs et al., 2016). During both growth events, the average ultrafine particle number concentrations were much larger (Event 1: 1200 cm^{-3}; Event 2: 2600 cm^{-3}) than those measured during the other "clean" periods in the campaign (250 cm^{-3}), suggesting that these growing particles are significant contributors to the ultrafine particle population during "clean" periods, which accounted for ~35 % of the measurement period. A prior analysis of ultrafine particle growth rates observed at the NOAA Research Station at Utqiagvik characterized these two growth events as "marine influenced" along with possible influence from Prudhoe Bay (Kolesar et al., 2017). To provide additional insights into the origins of these air masses, 72-hour HYSPLIT back trajectories were calculated for the period of each event before their arrival at the measurement site and are overlaid over MODIS satellite images of the region in Figure 5. There were no significant changes in the sea ice in this region over the time periods of the back trajectories, so the satellite image shown, while from 11 March, is representative of the entire modeling period (9 – 14 March). Two traces are shown for each event, with the starting point of the back trajectory corresponding to the beginning and halfway time points of the events. The black boxes on Figure 5 indicate areas of direct ocean-atmosphere interfaces in the sea ice, both in the form of open leads, which are small regions of water between ice sheets that serve as direct interfaces between the

ocean and atmosphere, and open ocean. Sea ice leads have been shown to contribute to sea spray and seawater-like particles in the atmosphere (May et al., 2016; Nilsson et al., 2001). The back trajectories for the air masses associated with both events originate in the same region of the Arctic Ocean, however there are differences in their geographic paths and altitudes. The air masses associated with Event 1 did not pass over the leads offshore of Prince Patrick Island (Northwest Territories, Canada) and spent more time aloft, at ~350 m above ground level (AGL) which is near the top of the estimated boundary layer during this time (Boylan et al., 2014), reaching surface level 24 hours before the start of the observed event. The air masses impacting Event 2 passed over open leads off Prince Patrick Island and are much closer to the surface (not exceeding 150 m AGL over the 72 hours), opening up the possibility that the source of the species responsible for nucleation and/or growth came from these leads. Given the chemical complexity of the marine upper boundary layer compared to near the surface (Zheng et al., 2021), the species involved in particle growth are likely to be different for these two events. A prior study in the remote marine atmosphere observed higher sulfuric acid in the free troposphere compared to the boundary layer (Clarke et al., 1998). That study attributed higher sulfuric acid aloft to cloud-pumping of precursor compounds, lower scavenging aloft due to low particle concentrations, and cloud-induced enhancements of actinic flux and associated OH production.

Reanalysis data was used to estimate wind speeds at the open leads to assess the potential role of primary sea spray in forming the initial seeds for condensational growth (Global Modeling and Assimilation Office (GMAO), 2015). When wind speeds exceed 4 m s^{-1} over open water, breaking waves tend to produce sea spray aerosol (May et al., 2016; Nilsson et al., 2001). This phenomenon has been previously observed at Utqiagvik in the winter in sub-500 nm particles (Kirpes et al., 2018, 2019). While the air masses for Event 2 were passing over the open leads, wind speeds ranged from 4.0 – 5.5 m s^{-1} over the open leads, averaging a speed of 4.8 m s^{-1}. Such speeds would be sufficient to produce sea spray aerosol, supporting the hypothesis that they were initial seeds for condensational growth during Event 2.

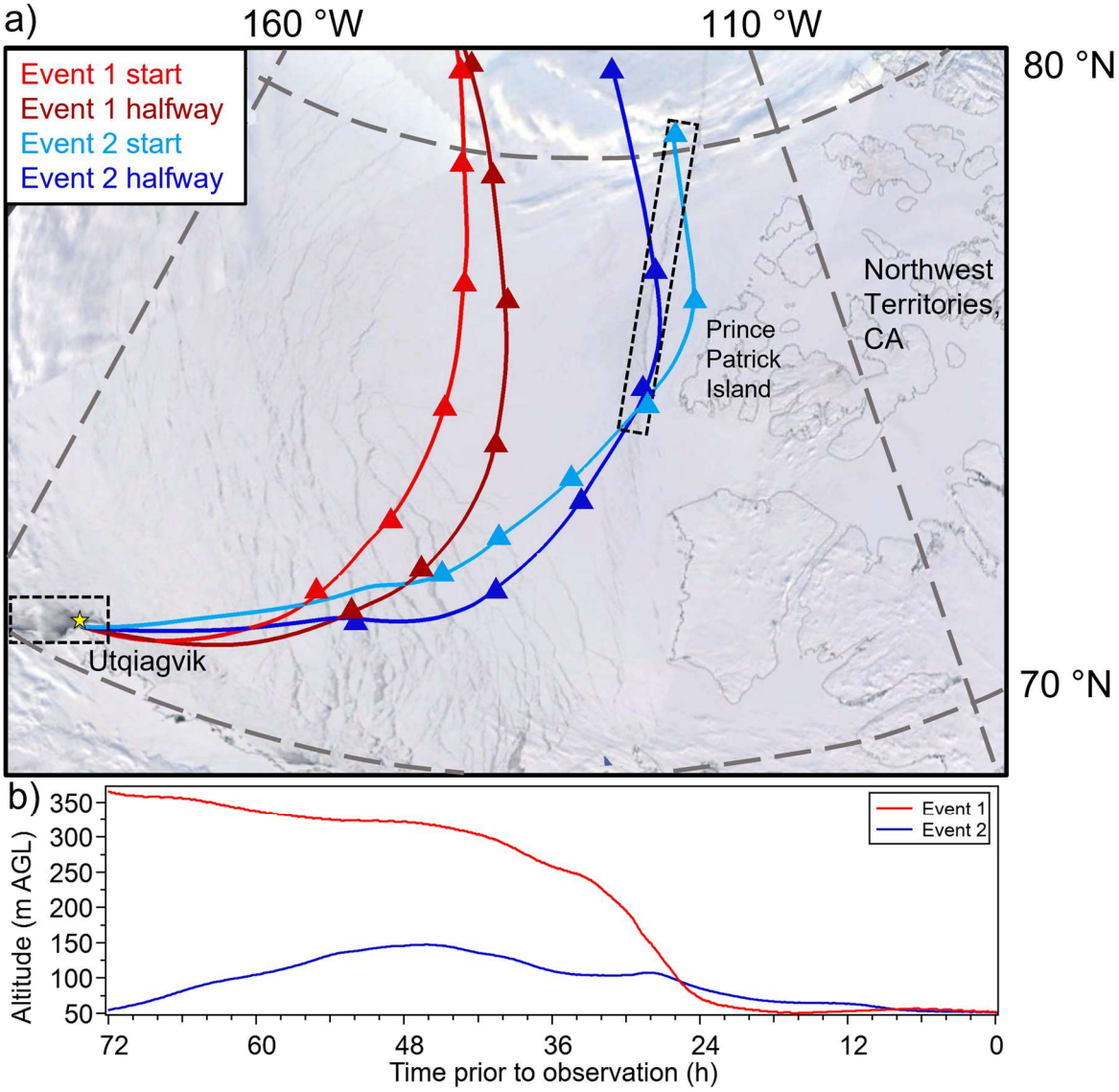

Figure 5. Air mass back trajectory analysis for each growth event. (a) HYSPLIT 72-hour back trajectories for each event plotted with corrected-reflectance MODIS satellite images from March 11, with one trajectory at the beginning of each event and one halfway through growth. Triangles mark 12-hour time points. The blue region in the upper-left corner is an imaging artefact and does not represent open ocean. Black boxes highlight regions with sea ice leads. (b) Average altitudes above ground level (AGL) of the two trajectories calculated for each event.

Using the SICIMS measurements, we estimated the contribution to the measured growth rate at the measurement site from condensation of H_2SO_4 using the equation provided in Kuang et al. (2010) for Γ, the fraction of growth that can be attributed to H_2SO_4 condensation:

$$\Gamma = \frac{2GR_{meas}}{v_1[H_2SO_4]\bar{c}_1} \qquad (4)$$

where GR_{meas} is the measured growth rate (nm h^{-1}), $[H_2SO_4]$ is the average number concentration of H_2SO_4 measured onsite during the event (molecules cm^{-3}), ν_1 is the volume of a hydrated H_2SO_4 molecule (1.7 x 10^{-22} cm^3), and $\bar{c}_1$ is the mean thermal speed of the condensing H_2SO_4 monomer (nm hr^{-1}). From the Γ calculations, the results of which are summarized in Table 1, we estimate that H_2SO_4 condensation accounted for 22% of volumetric growth during Event 1 (Γ = 4.5 ± 1.5) and did not contribute substantially to Event 2 (Γ = 139.2 ± 4.2). The Γ analysis assumes that the concentration of H_2SO_4 measured during each event represents that which sustained growth during the entire period of growth. It thus assumes that the air mass is exposed to a constant supply of condensing H_2SO_4 and overlooks the role of inhomogeneities during growth (Kivekäs et al., 2016). Nonetheless, the distinct differences in growth rates and apparent influence from H_2SO_4 on observed particle growth are evidence of fundamental differences in the species and circumstances responsible for the observed events. The SSA measured for bulk aerosol during these events were very similar, suggesting the differences in these events were not impacting larger particle radiative properties.

Table 1. Ultrafine particle growth rates and H_2SO_4 contribution to growth (Γ)

Event	T (°C)	GR_{meas} (nm h^{-1})	Γ	$[H_2SO_4]$ (cm^{-3})
1 (12 March)	-26.4	0.9 ± 0.1	4.5 ± 1.5	3.7 x 10^6
2 (13 – 14 March)	-27.6	2.1 ± 0.1	139.2 ± 4.2	3.0 x 10^5

To further investigate the composition of the particles in each growth event, we next consider the indirect measurements of UFP composition. Figure 6 shows 15 and 35 nm diameter *HGF* data for the two events. An instrument malfunction resulted in missing 15 nm data during Event 1; that issue was resolved midway through Event 2 but as a result we were only able to obtain one reliable measurement of 15 nm *HGF* during that event. Based on the size distribution measurements shown in Figure 4, we postulate that 35 nm particle composition represents both background particles as well as those associated with the growth events. While the condensing species are likely similar for both particle populations, prior studies suggest a higher salt content in larger particles compared to smaller ones if these events began as primary marine aerosol (Prather et al., 2013). Figure 6a shows both the average *HGF* distributions measured during the growth events and the Gaussian fit to each distribution. The sampled particles in both growth events were highly hygroscopic. The *HGF* for 35 nm diameter particles measured during Event 1 was 2.10 ± 0.12. *HGFs* of 15 nm and 35 nm diameter particles during Event 2 were 1.65 and 1.94 ± 0.08, respectively. Measured *HGFs* of 35 nm particles are significantly higher than those measured during the background period (Figure 2c), even compared to the period during 29 March when $[H_2SO_4]$ was similarly high. This difference is evidence of a compositional difference between the particles generated

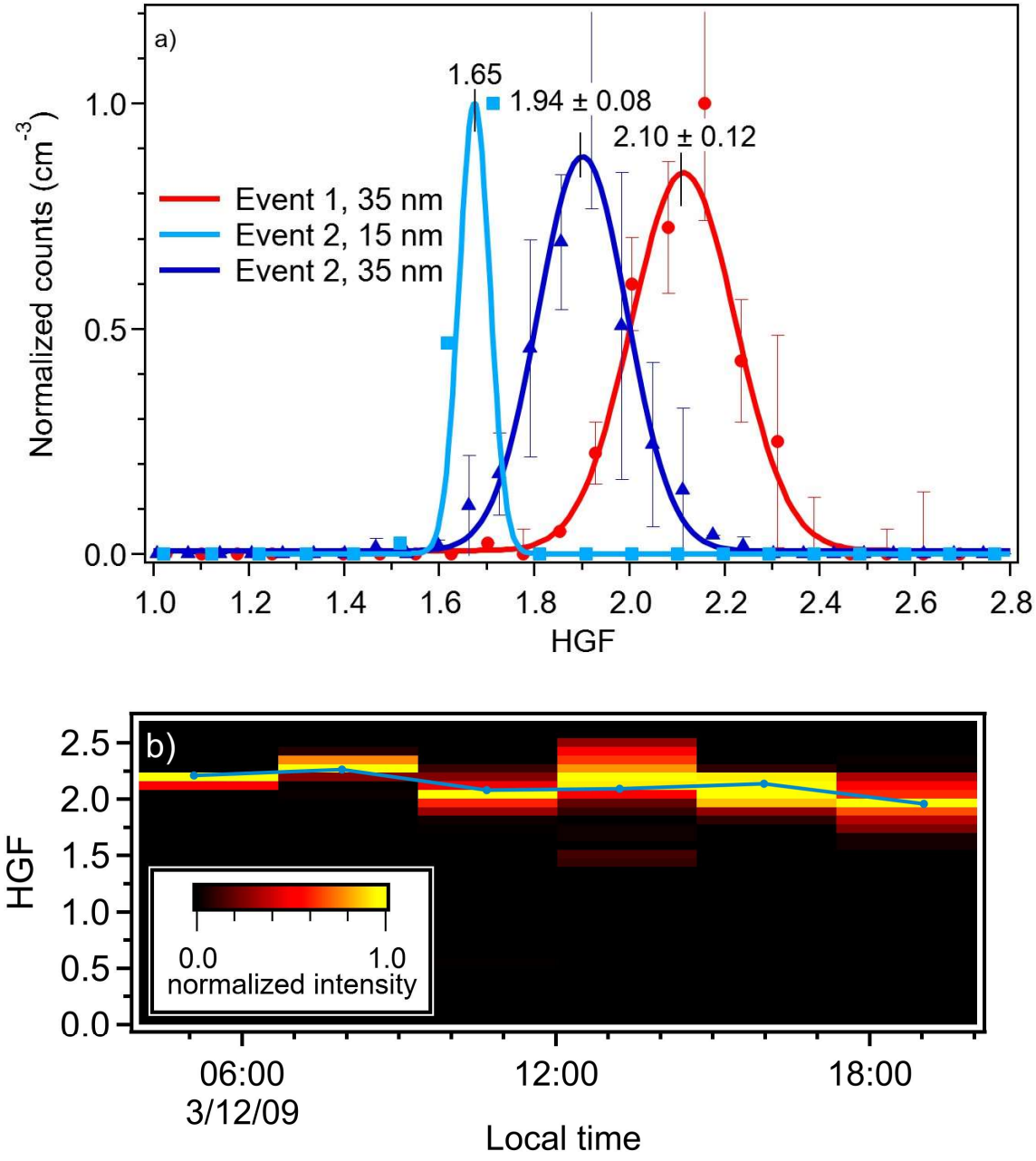

Figure 6. (a) Measured *HGF*s at 90% RH for 15 and 35 nm size-selected particles during each event (15 nm data missing for Event 1). Markers are the averaged size distributions measured during each event. The error bars represent standard deviation and the number of measurements at each size is shown in the legend. Solid lines are Gaussian fits of the data. Distributions were normalized prior to plotting to facilitate comparison. (b) Time evolution of Event 1 *HGF*. The Event 2 *HGF* distribution did not change during the growth period.

in these two formation events and the background ultrafine particles at the site, and we hypothesize that the former was highly influenced by primary marine particle production whereas the latter is more

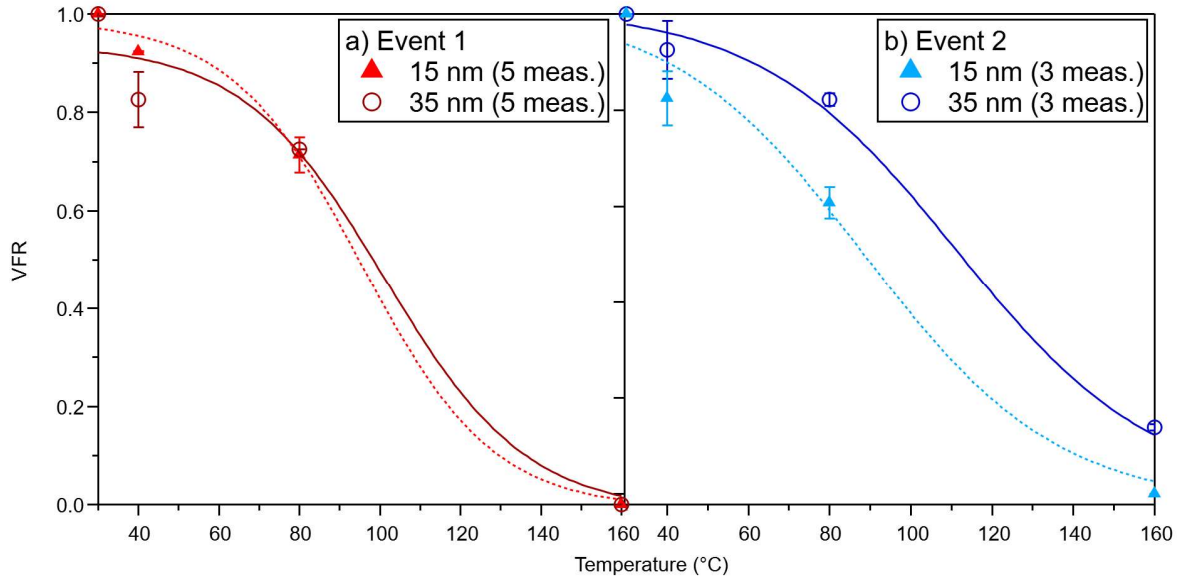

Figure 7. Volume fraction remaining at 40, 80, and 160 °C for 15 and 35 nm size-selected particles during (a) Event 1 and (b) Event 2. The error bars represent standard deviation and the number of measurements at each size is shown in the legend. Initial volume was assumed to be the volume at 30 °C.

representative of aged sulfate and organics as discussed above. The 35 nm *HGFs* measured for both events are smaller than those previously reported for 50 nm mobility-selected sea salt particles (*HGF* = 2.2) (Zieger et al., 2017) but fall in the range of nebulized 40 nm sea water proxy with concentrations of organic material representative of biological activity (*HGF* = 1.9 – 2.3, see Figure 2c) (Fuentes et al., 2011) and are larger than that of 35 nm ammonium sulfate (*HGF* = 1.65) (Hämeri et al., 2000). Figure 6b shows that, during Event 1, 35 nm particle *HGF* slowly decreased from 2.20 to 1.95. Within measurement uncertainty, the *HGF* at the end of Event 1 corresponds to the average *HGF* measured during Event 2 (1.94 ± 0.08), the latter of which remained relatively constant throughout its shorter 4-hour period of growth. The *HGF* distribution of 15 nm particles sampled during Event 2 is narrower than those of 35 nm particles, which indicates that 15 nm particles were compositionally more homogeneous compared to 35 nm particles. The peak *HGF* for 15 nm particles, 1.65, is lower than that measured for 35 nm particles, in part due to the Kelvin effect but also likely because of the relatively smaller contribution of primary marine particle seeds to overall particle composition.

Figure 7 shows volatility measurements of 15 and 35 nm mobility-selected particles collected during the events. We note first that the *VFR* data are very similar for both particle sizes measured in Event 1, whereas Event 2 shows more substantial differences between the two sizes. One possible explanation for this can be seen in Figure 4, in which the size distribution of Event 1 (Figure 4a) appears to have a single mode and relatively low concentration of particles larger than 30 nm. In contrast, Event 2 (Figure 4b) occurs with overall higher concentrations of particles larger than 30 nm in diameter.

Considering the exceptionally high measured *HGF* measured during both events, it is likely that the differences in *VFR* during Event 2 arise from differences in the relative contributions of primary marine aerosol. In Event 1, 15 nm UFP volume is almost completely lost at 160 °C whereas, in Event 2, 15 nm particles appear to be somewhat less volatile. While generally it is true that background particles show similar volatility at 160 °C (see Figure 3), there is a notable difference in size-dependence of the *VFR* data from these events compared to that of the background period. For the latter, heating to 80 °C resulted in 19.2 ± 0.2 % *VFR* for 35 nm particles, whereas during Event 1, *VFRs* of 71 ± 4 % were measured for 15 nm and 72.57 ± 0.01 % 35 nm diameter particles. Event 2 showed a similar behavior, with *VFR* of 61 ± 3 % for 15 nm particles and 82 ± 1 % for 35 nm particles. Thus, compared to background particles, those associated with these UFP formation events were significantly less volatile at 80 °C. We attribute this difference in *VFR* at 80 °C to the relative contributions of organics and a low-volatility salt, which in the case of the former is reported as ~40 % for laboratory-generated α-pinene SOA (Huffman et al., 2009) and for the latter as ~100 % for ammonium sulfate and sodium chloride (Huffman et al., 2008; Villani et al., 2007).

To summarize the observations of the two UFP growth events, both events display qualities of regional new particle formation events, specifically sustained and continuous growth that persisted for several hours. This suggests that particles formed over a large region and then were advected over the measurement site, with the first particles detected corresponding to the least aged and the last ones the most aged. Both events are characterized by higher *HGFs* than can be achieved by sulfate salts, and from this we conclude that particles contained significant amounts of highly hygroscopic salts. These salts typically have lower volatility than ammoniated sulfate. The high *HGF* measured are consistent with sea salt consisting of NaCl and other trace elements, which is expected to be non-volatile at 160 °C (Mendes et al., 2016; Villani et al., 2007). The non-volatile nature of NaCl was confirmed for 15 nm particles in laboratory tests with our thermodenuder. Our measurements of 15 and 35 nm *VFR* at 80 °C are consistent with published values for 25 nm *VFR* of marine nanoparticles sampled in Antarctica (Asmi et al., 2010) and observations of 50 nm diameter particle volatility the Arctic and Pacific Oceans (Kim et al., 2015). They are also consistent with reported 30-40 nm particle volatility performed in the North Atlantic (Quinn et al., 2019) and coastal California (Bates et al., 2012), although those observations were performed at higher temperatures (230 °C). Our observations of the importance of a component more hygroscopic than ammonium sulfate in nanoparticle composition is inconsistent with the main conclusions of a study of nanoparticle volatility performed at Svalbard by Giamarelou, et al. (2016), who concluded that ammoniated sulfates dominated 12 nm particle compositon. That study, which did not have supporting hygroscopicity measurements nor direct measurements of sulfuric acid, based its conclusion on the observation that ambient particles completely volatilized at 230 °C. The results for Event 2 are consistent

with a comprehensive study by Clarke et al., (2006), which concluded that marine UFPs contained a non-volatile core with as much as 90 % by volume of a component that completely volatilized at 300 °C. We hypothesize that the newly formed UFPs observed in this study are comprised of a mixture of volatile organic species and a salt with hygroscopicity similar to sea salt or NaCl, but that largely volatilizes by 160 °C. We are not aware of any aerosol component that has this property but hope that future observations can shed light on this intriguing property of newly formed particles in this region.

Our estimates of volume fraction based on the measured *HGFs* during these events are separated into the composition of 15 nm particles during Event 2, which minimizes potential biases from background particles and is therefore more representative of the species responsible for this event, and that of 35 nm particles during both events, which we hypothesize as being influenced by larger seed particles and higher levels of background particles. For the analysis of 35 nm particle composition, we consider a mixture of sea salt (*HGF* = 2.2), sulfuric acid (*HGF* = 1.9), and oxidized organic (*HGF* = 1.2). We acknowledge that our volatility observations may rule out sea salt but this is the only component that we are aware of that could be responsible for the high *HGFs* observed in this study and so we apply it to this analysis with the caveat that this component has this *HGF* but cannot be pure NaCl. Our Γ analysis (see Table 1) suggests that sulfuric acid may contribute to 22% of particulate volume during Event 1, and we use this information to constrain the contribution by sulfuric acid to composition during that event. For the analysis of 15 nm particle composition during Event 2, we use the following *HGFs* from prior studies: sea salt (*HGF* = 2.0) (Zieger et al., 2017) and oxidized organic (*HGF* = 1.1) (Virkkula et al., 1999). Table 2 summarizes the results of the analysis of these *HGF* measurements by the ZSR method. During both Events 1 and 2, 35 nm diameter particles contained significant amounts of the very hygroscopic “sea salt", with an estimated volume fraction (ε_{SS}) of 0.74. The balance of composition is predominantly sulfuric acid for Event 1 (ε_{SA} = 0.22), and oxidized organic for Event 2 (ε_{ORG} = 0.26). Oxidized organics contributed a small amount to 35 nm particle composition in Event 1 (ε_{ORG} = 0.04). Even though these results are based on measured *HGF*, they are qualitatively in agreement with the measurements of volatility if it were true that the oxidized organics were of low volatility. This possibility is also suggested in the study of Arctic aerosol volatility by Giamarelou et al. (2016). Finally, the significant contribution of “sea salt” to 35 nm particle composition in both events agrees qualitatively with the analyses of the size distribution, back trajectories and wind data, all of which point to the likelihood that marine emissions were responsible for the initiation of these events. As for the 15 nm diameter particles most associated with the UFP growth event, our analysis suggests that this event may have also begun with the formation of primary hygroscopic sea salt-like particles, and then subsequently grew from the condensation of organic compounds. As mentioned previously, Event 2 was first observed at the site with a measured modal diameter of 7 nm, so while this qualitatively agrees with the *HGF*

measurements that suggest a sea salt-like core, the *HGF* measurements suggest a much higher volume fraction. The high values of *HGF* measured during both events indicates their potential to act as CCN (Petters & Kreidenweis, 2007), thus contributing to the radiative budget in this region. Previous work has attributed CCN in the Arctic spring to haze (Jung et al., 2018), though these results highlight the need for further study of newly-formed ultrafine particles in the Arctic during this time of year to further investigate the properties contributing to CCN formation and the resulting radiative forcing effects.

Table 2. Estimates of the volume fraction of representative compound classes during UFP formation events, based on analysis of HGF data using the ZSR mixing rule. ε_{SS}: volume fraction of hygroscopic sea salt, ε_{SA}: volume fraction of sulfuric acid, ε_{ORG}: volume fraction of organic compounds.

Event	Dp (nm)	ε_{SS}	ε_{SA}	ε_{ORG}
1 (12 March)	35	0.74	0.22	0.04
2 (13 – 14 March)	15	0.63	0	0.37
	35	0.74	0	0.26

4 Conclusion

In this manuscript, we report indirect composition measurements of ultrafine particles in Utqiagvik, Alaska, observed during late winter and early spring (5 March – 14 April 2009). Our estimates of size-resolved particle composition combine measurements of particle hygroscopicity and volatility with those of gas-phase sulfuric acid. During "background" periods with minimal local anthropogenic influence, ultrafine particles in this region were characterized by low concentrations, averaging 380 cm^{-3}, especially sub-20 nm diameter particles, which had an average number concentration of 60 cm^{-3}. Under these conditions, particles exhibited moderate hygroscopic growth that suggests a mixed organic-inorganic composition. Volatility measurements support this observation, with less than 20% *VFR* measured for sub-100 nm particles. We estimated the volume fractions of representative compounds using the ZSR method and found that ammoniated sulfate (~30% by volume) and low-hygroscopicity oxidized organics (~70% by volume) could account for the measured hygroscopicity of 35 nm particles. Gas-phase H_2SO_4 generally trends with solar radiation but did not follow a regular diurnal pattern in this campaign. We also analyzed two ultrafine particle growth events wherein the properties of the particles differed greatly from those measured during the background period. Both growth events produced highly hygroscopic particles, but the differences in the average measured hygroscopic growth factors (Event 1: 2.1; Event 2: 1.9), as well as growth rates and H_2SO_4 contributions to growth, suggest differences in their chemical composition. HYSPLIT back trajectories and MODIS satellite imagery suggest that Event 1 was

likely influenced by upper marine boundary layer processes, while Event 2 passed over open leads in the lower boundary layer. Both hygroscopicity and volatility data show that particles in both growth events contain a significant volume fraction of high hygroscopicity, low volatility species and support a role for primary marine emissions similar to sea salt as the initial seed for these events. The preponderance of evidence suggests that Event 1 particles were composed of mixtures of sea salt-like species and sulfuric acid, whereas Event 2 particles contained similar levels of salt but the balance of the composition was oxidized organics. This sea salt-like species, which is highly hygroscopic but more volatile than NaCl, is not known and illustrates the necessity of further measurements in this region. This study illuminates the importance of a multi-pronged approach to indirect measurements of ultrafine particle composition and illustrates the variability that exists between background aerosol and newly formed aerosol. It also highlights the potentially important role of low-volatility, high-hygroscopicity primary marine species like sea salt as initiators of ultrafine particle production in the Arctic late-winter, which can significantly impact CCN concentrations and thus climate, in this sensitive region. Prior measurements of CCN during this tune of year have focused primarily on Arctic Haze, though new particle formation and growth of primary ultrafine particles may be an important source of CCN. Additional measurements of nanoparticle growth events during this time of year should be performed to better elucidate the processes driving particle production in this important region.

Acknowledgement

The authors wish to thank the organizers of the OASIS 2009 field campaign, the Barrow Arctic Science Consortium for logistics support, and all of the researchers who contributed to the campaign. The authors gratefully acknowledge funding for the PASS-1 deployment analysis of this dataset by the Department of Energy, grant DE- SC0019000DOE, DE-SC0019000 and KP1701000.

Data Availability Statement

All relevant data from the OASIS Barrow 2009 field campaign are publicly available at the following DOIs: 10.5065/D6P8491K (aerosol measurements), 10.5065/D6TM787P (OH and H_2SO_4), 10.5065/D62J6902 (meteorology) and 10.7280/D15X1J (HTDMA, VTDMA, and SSA measurements for the periods highlighted in this manuscript).

References

Abbatt, J. P. D., Leaitch, W. R., Aliabadi, A. A., Bertram, A. K., Blanchet, J.-P., Boivin-Rioux, A., et al. (2019). Overview paper: New insights into aerosol and climate in the Arctic. *Atmospheric Chemistry*

and Physics, *19*. https://doi.org/10.5194/acp-19-2527-2019

Allan, J. D., Williams, P. I., Najera, J., Whitehead, J. D., Flynn, M. J., Taylor, J. W., et al. (2015). Iodine observed in new particle formation events in the Arctic atmosphere during ACCACIA. *Atmospheric Chemistry and Physics*, *15*(10), 5599–5609. https://doi.org/10.5194/acp-15-5599-2015

Asmi, E., Frey, A., Virkkula, A., Ehn, M., Manninen, H. E., Timonen, H., et al. (2010). Hygroscopicity and chemical composition of Antarctic sub-micrometre aerosol particles and observations of new particle formation. *Atmospheric Chemistry and Physics*, *10*, 4253–4271. https://doi.org/10.5194/acp-10-4253-2010

Asmi, E., Kondratyev, V., Brus, D., Laurila, T., Lihavainen, H., Backman, J., et al. (2016). Aerosol size distribution seasonal characteristics measured in Tiksi, Russian Arctic. *Atmospheric Chemistry and Physics*, *16*(3), 1271–1287. https://doi.org/10.5194/acp-16-1271-2016

Assmy, P., Fernández-Méndez, M., Duarte, P., Meyer, A., Randelhoff, A., Mundy, C. J., et al. (2017). Leads in Arctic pack ice enable early phytoplankton blooms below snow-covered sea ice. *Scientific Reports*, *7*(1), 1–9. https://doi.org/10.1038/srep40850

Baccarini, A., Karlsson, L., Dommen, J., Duplessis, P., Vüllers, J., Brooks, I. M., et al. (2020). Frequent new particle formation over the high Arctic pack ice by enhanced iodine emissions. *Nature Communications*, *11*(1). https://doi.org/10.1038/s41467-020-18551-0

Barrie, L. A. (1986). Arctic air pollution: An overview of current knowledge. *Atmospheric Environment*, *20*(4), 643–663. https://doi.org/10.1016/0004-6981(86)90180-0

Bates, T. S., Quinn, P. K., Frossard, A. A., Russell, L. M., Hakala, J., Petäjä, T., et al. (2012). Measurements of ocean derived aerosol off the coast of California. *Journal of Geophysical Research Atmospheres*, *117*(12), 0–15. https://doi.org/10.1029/2012JD017588

Bergin, M. H., Ogren, J. A., Schwartz, S. E., & Mcinnes, L. M. (1997). Evaporation of ammonium nitrate aerosol in a heated nephelometer: Implications for field measurements. *Environmental Science and Technology*, *31*(10), 2878–2883. https://doi.org/10.1021/es970089h

Biskos, G., Paulsen, D., Russell, L. M., Buseck, P. R., & Martin, S. T. (2006). Prompt deliquescence and efflorescence of aerosol nanoparticles. *Atmospheric Chemistry and Physics*, *6*(12), 4633–4642. https://doi.org/10.5194/acp-6-4633-2006

Bodhaine, B. A., Harris, J. M., & Herbert, G. A. (1981). Aerosol light scattering and condensation nuclei measurements at Barrow, Alaska. *Atmospheric Environment*, *15*(8), 1375–1389. https://doi.org/10.1016/0004-6981(81)90344-9

Boylan, P., Helmig, D., Staebler, R., Turnipseed, A., Fairall, C., & Neff, W. (2014). Boundary layer dynamics during the Ocean-Atmosphere-Sea-Ice-Snow (OASIS) 2009 experiment at Barrow, AK. *Journal of Geophysical Research: Atmospheres*, *119*(5), 2261–2278. https://doi.org/10.1002/2013JD020299

Browse, J., Carslaw, K. S., Arnold, S. R., Pringle, K., & Boucher, O. (2012). The scavenging processes controlling the seasonal cycle in Arctic sulphate and black carbon aerosol. *Atmospheric Chemistry and Physics*, *12*(15), 6775–6798. https://doi.org/10.5194/acp-12-6775-2012

Burkart, J., Hodshire, A. L., Mungall, E. L., Pierce, J. R., Collins, D. B., Ladino, L. A., et al. (2017). Organic Condensation and Particle Growth to CCN Sizes in the Summertime Marine Arctic Is Driven by Materials More Semivolatile Than at Continental Sites. *Geophysical Research Letters*, *44*(20), 10,725-10,734. https://doi.org/10.1002/2017GL075671

Burtscher, H., Baltensperger, U., Bukowiecki, N., Cohn, P., Hüglin, C., Mohr, M., et al. (2001). Separation of volatile and non-volatile aerosol fractions by thermodesorption: Instrumental development and applications. *Journal of Aerosol Science*, *32*(4), 427–442. https://doi.org/10.1016/S0021-8502(00)00089-6

Chang, R. Y. W., Sjostedt, S. J., Pierce, J. R., Papakyriakou, T. N., Scarratt, M. G., Michaud, S., et al. (2011). Relating atmospheric and oceanic DMS levels to particle nucleation events in the Canadian Arctic. *Journal of Geophysical Research Atmospheres*, *116*(21). https://doi.org/10.1029/2011JD015926

Chen, H., Cheng, T., & Wu, Y. (2014). Effects of morphology on the radiative properties of internally mixed light absorbing carbon aerosols with different aging status. *Optics Express*, *22*(13), 15904–15917. https://doi.org/10.1364/OE.22.015904

Clarke, A. D., Charlson, R. J., & Radke, L. F. (1984). Airborne observations of Arctic aerosol, IV: Optical properties of Arctic haze. *Geophysical Research Letters*, *11*(5). https://doi.org/10.1029/GL011i005p00405

Clarke, A. D., Varner, J. L., Eisele, F., Mauldin, R. L., Tanner, D., & Litchy, M. (1998). Particle production in the remote marine atmosphere: Cloud outflow and subsidence during ACE-1. *Journal of Geophysical Research Atmospheres*, *103*(D13), 16,397-16,409.

Clarke, A. D., Owens, S. R., & Zhou, J. (2006). An ultrafine sea-salt flux from breaking waves: Implications for cloud condensation nuclei in the remote marine atmosphere. *Journal of Geophysical Research*, *111*(D6), D06202. https://doi.org/10.1029/2005JD006565

Cochran, R. E., Ryder, O. S., Grassian, V. H., & Prather, K. A. (2017). Sea spray aerosol: The chemical link between the oceans, atmosphere, and climate. *Accounts of Chemical Research*. https://doi.org/10.1021/acs.accounts.6b00603

Collins, D. B., Burkart, J., Y-W Chang, R., Lizotte, M., Boivin-Rioux, A., Blais, M., et al. (2017). Frequent ultrafine particle formation and growth in Canadian Arctic marine and coastal environments. *Atmospheric Chemistry and Physics*, *17*, 13119–13138. https://doi.org/10.5194/acp-17-13119-2017

Covert, D. S., & Heintzenberg, J. (1993). Size distributions and chemical properties of aerosol at Ny Ålesund, Svalbard. *Atmospheric Environment Part A, General Topics*, *27*(17–18), 2989–2997. https://doi.org/10.1016/0960-1686(93)90331-R

Cravigan, L. T., Mallet, M. D., Vaattovaara, P., Harvey, M. J., Law, C., Modini, R., et al. (2020). Sea spray aerosol organic enrichment, water uptake and surface tension effects. *Atmospheric Chemistry and Physics*, *20*(13), 7955–7977. https://doi.org/10.5194/ACP-20-7955-2020

Creamean, J. M., Maahn, M., De Boer, G., McComiskey, A., Sedlacek, A. J., & Feng, Y. (2018). The influence of local oil exploration and regional wildfires on summer 2015 aerosol over the North Slope of Alaska. *Atmospheric Chemistry and Physics*, *18*(2), 555–570. https://doi.org/10.5194/ACP-18-555-2018

Croft, B., Martin, R. V, Leaitch, W. R., Tunved, P., Breider, T. J., D'Andrea, S. D., & Pierce, J. R. (2016). Processes controlling the annual cycle of Arctic aerosol number and size distributions. *Atmospheric Chemistry and Physics*, *16*, 3665–3682. https://doi.org/10.5194/acp-16-3665-2016

Croft, B., Martin, R. V, Richard Leaitch, W., Burkart, J., Y-W Chang, R., Collins, D. B., et al. (2019). Arctic marine secondary organic aerosol contributes significantly to summertime particle size distributions in the Canadian Arctic Archipelago. *Atmospheric Chemistry and Physics*, *19*, 2787–

2812. https://doi.org/10.5194/acp-19-2787-2019

Dal Maso, M., Kulmala, M., Riipinen, I., Wagner, R., Hussein, T., Aalto, P. P., & Lehtinen, K. E. J. (2005). Formation and growth of fresh atmospheric aerosols: Eight years of aerosol size distribution data from SMEAR II, Hyytiälä, Finland. *Boreal Environment Research*, *10*(5), 323–336.

Dall'Osto, M., Beddows, D. C. S., Tunved, P., Krejci, R., Ström, J., Hansson, H. C., et al. (2017). Arctic sea ice melt leads to atmospheric new particle formation. *Scientific Reports*, *7*(1), 1–10. https://doi.org/10.1038/s41598-017-03328-1

Dall'Osto, M., Simo, R., Harrison, R. M., Beddows, D. C. S., Saiz-Lopez, A., Lange, R., et al. (2018). Abiotic and biotic sources influencing spring new particle formation in North East Greenland. *Atmospheric Environment*, *190*, 126–134. https://doi.org/10.1016/j.atmosenv.2018.07.019

Dall'Osto, M., Geels, C., Beddows, D. C. S., Boertmann, D., Lange, R., Nøjgaard, J. K., et al. (2018). Regions of open water and melting sea ice drive new particle formation in North East Greenland. *Scientific Reports*, *8*(1), 1–10. https://doi.org/10.1038/s41598-018-24426-8

Delene, D. J., & Ogren, J. A. (2002). Variability of aerosol optical properties at four North American surface monitoring sites. *Journal of the Atmospheric Sciences*, *59*(6), 1135–1150. https://doi.org/10.1175/1520-0469(2002)059<1135:VOAOPA>2.0.CO;2

Eisele, F. L., & Tanner, D. J. (1991). Ion-assisted tropospheric OH measurements. *Journal of Geophysical Research*, *96*(D5), 9295–9308. https://doi.org/10.1029/91JD00198

Eisele, F. L., & Tanner, D. J. (1993). Measurement of the gas phase concentration of H2SO4 and methane sulfonic acid and estimates of H2SO4 production and loss in the atmosphere. *Journal of Geophysical Research: Atmospheres*, *98*(D5). https://doi.org/10.1029/93JD00031

Ferek, R. J., Hobbs, P. V., Radke, L. F., Herring, J. A., Sturges, W. T., & Cota, G. F. (1995). Dimethyl sulfide in the Arctic atmosphere. *Journal of Geophysical Research*, *100*(D12), 26093–26104. https://doi.org/10.1029/95jd02374

Flowers, B. A., Dubey, M. K., Mazzoleni, C., Stone, E. A., Schauer, J. J., Kim, S. W., & Yoon, S. C. (2010). Optical-chemical-microphysical relationships and closure studies for mixed carbonaceous aerosols observed at Jeju Island; 3-laser photoacoustic spectrometer, particle sizing, and filter analysis. *Atmospheric Chemistry and Physics*, *10*(21), 10387–10398. https://doi.org/10.5194/acp-10-10387-2010

Freud, E., Krejci, R., Tunved, P., Leaitch, R., Nguyen, Q. T., Massling, A., et al. (2017). Pan-Arctic aerosol number size distributions: Seasonality and transport patterns. *Atmospheric Chemistry and Physics*, *17*(13), 8101–8128. https://doi.org/10.5194/ACP-17-8101-2017

Frieß, U., Sihler, H., Sander, R., Phler, D., Yilmaz, S., & Platt, U. (2011). The vertical distribution of BrO and aerosols in the Arctic: Measurements by active and passive differential optical absorption spectroscopy. *Journal of Geophysical Research Atmospheres*, *116*(18). https://doi.org/10.1029/2011JD015938

Frossard, A. A., Shaw, P. M., Russell, L. M., Kroll, J. H., Canagaratna, M. R., Worsnop, D. R., et al. (2011). Springtime Arctic haze contributions of submicron organic particles from European and Asian combustion sources. *Journal of Geophysical Research-Atmospheres*, *116*. https://doi.org/10.1029/2010jd015178

Frossard, A. A., Russell, L. M., Massoli, P., Bates, T. S., & Quinn, P. K. (2014). Side-by-side comparison of four techniques explains the apparent differences in the organic composition of generated and ambient marine aerosol particles. *Aerosol Science and Technology*, *48*(3), v–x.

https://doi.org/10.1080/02786826.2013.879979

Fuentes, E., Coe, H., Green, D., & McFiggans, G. (2011). On the impacts of phytoplankton-derived organic matter on the properties of the primary marine aerosol - Part 2: Composition, hygroscopicity and cloud condensation activity. *Atmospheric Chemistry and Physics*, *11*(6), 2585–2602. https://doi.org/10.5194/acp-11-2585-2011

Garrett, T. J., Brattström, S., Sharma, S., Worthy, D. E. J., & Novelli, P. (2011). The role of scavenging in the seasonal transport of black carbon and sulfate to the Arctic. *Geophysical Research Letters*, *38*(16). https://doi.org/10.1029/2011GL048221

Ghahremaninezhad, R., Norman, A.-L., Abbatt, J. P. D., Levasseur, M., & Thomas, J. L. (2016). Biogenic, anthropogenic and sea salt sulfate size-segregated aerosols in the Arctic summer. *Atmospheric Chemistry and Physics*, *16*(8), 5191–5202. https://doi.org/10.5194/acp-16-5191-2016

Giamarelou, M., Eleftheriadis, K., Nyeki, S., Tunved, P., Torseth, K., & Biskos, G. (2016). Indirect evidence of the composition of nucleation mode atmospheric particles in the high Arctic. *Journal of Geophysical Research: Atmospheres*, *121*(2), 965–975. https://doi.org/10.1002/2015JD023646

Global Modeling and Assimilation Office (GMAO). (2015). MERRA-2 inst3_3d_asm_Np: 3d,3-Hourly,Instantaneous,Pressure-Level,Assimilation,Assimilated Meteorological Fields V5.12.4, Greenbelt, MD, USA, Goddard Earth Sciences Data and Information Services Center (GES DISC), Accessed 8/23/2021. https://doi.org/10.5067/QBZ6MG944HW0

Gysel, M., Weingartner, E., Nyeki, S., Paulsen, D., Baltensperger, U., Galambos, I., & Kiss, G. (2004). Hygroscopic properties of water-soluble matter and humic-like organics in atmospheric fine aerosol. *Atmospheric Chemistry and Physics*, *4*(1), 35–50. https://doi.org/10.5194/acp-4-35-2004

Gysel, M., McFiggans, G. B., & Coe, H. (2009). Inversion of tandem differential mobility analyser (TDMA) measurements. *Journal of Aerosol Science*, *40*(2). https://doi.org/10.1016/j.jaerosci.2008.07.013

Häkkinen, S. A. K., Äijälä, M., Lehtipalo, K., Junninen, H., Backman, J., Virkkula, A., et al. (2012). Long-term volatility measurements of submicron atmospheric aerosol in Hyytiälä, Finland. *Atmospheric Chemistry and Physics*, *12*(22), 10771–10786. https://doi.org/10.5194/acp-12-10771-2012

Hall, D. K., & Riggs, G. A. (2015). MODIS/Aqua Sea Ice Extent 5-Min L2 Swath 1km, Version 6 [March 2009]. Retrieved February 18, 2021, from https://doi.org/10.5067/MODIS/MYD29.006

Hämeri, K., Väkevä, M., Hansson, H.-C., & Laaksonen, A. (2000). Hygroscopic growth of ultrafine ammonium sulphate aerosol measured using an ultrafine tandem differential mobility analyzer. *Journal of Geophysical Research: Atmospheres*, *105*(D17), 22231–22242. https://doi.org/10.1029/2000JD900220

Hancke, K., Lund-Hansen, L. C., Lamare, M. L., Pedersen, S. H., King, M. D., Andersen, P., & Sorrell, B. K. (2018). Extreme Low Light Requirement for Algae Growth Underneath Sea Ice: A Case Study From Station Nord, NE Greenland. *Journal of Geophysical Research: Oceans*, *123*(2), 985–1000. https://doi.org/10.1002/2017JC013263

Hand, J. L., & Kreidenweis, S. M. (2002). A New Method for Retrieving Particle Refractive Index and Effective Density from Aerosol Size Distribution Data. *Aerosol Science and Technology*, *36*(10), 1012–1026.

Hawkins, L. N., & Russell, L. M. (2010). Polysaccharides, Proteins, and Phytoplankton Fragments: Four Chemically Distinct Types of Marine Primary Organic Aerosol Classified by Single Particle

Spectromicroscopy. *Advances in Meteorology*, *2010*, 1–14. https://doi.org/10.1155/2010/612132

Heintzenberg, J. (1982). Size-segregated measurements of particulate elemental carbon and aerosol light absorption at remote arctic locations. *Atmospheric Environment (1967)*, *16*(10), 2461–2469. https://doi.org/10.1016/0004-6981(82)90136-6

Heintzenberg, J., Leck, C., & Tunved, P. (2015). Potential source regions and processes of aerosol in the summer Arctic. *Atmospheric Chemistry and Physics*, *15*, 6487–6502. https://doi.org/10.5194/acp-15-6487-2015

Hinds. William C. (1999). Aerosol Technology: Properties, Behavior, and Measurement of Airborne Particles, 2nd Edition | Wiley. Retrieved May 17, 2021, from https://www.wiley.com/en-us/Aerosol+Technology%3A+Properties%2C+Behavior%2C+and+Measurement+of+Airborne+Particles%2C+2nd+Edition-p-9780471194101

Hoffman, J. P., Ackerman, S. A., Liu, Y., & Key, J. R. (2019). The Detection and Characterization of Arctic Sea Ice Leads with Satellite Imagers. *Remote Sensing 2019, Vol. 11, Page 521*, *11*(5), 521. https://doi.org/10.3390/RS11050521

Hoppel, W. A., Dinger, J. E., & Ruskin, R. E. (1973). Vertical Profiles of CCN at Various Geographical Locations. *Journal of the Atmospheric Sciences*, *30*(7). https://doi.org/10.1175/1520-0469(1973)030<1410:VPOCAV>2.0.CO;2

Huffman, J. A., Ziemann, P. J., Jayne, J. T., Worsnop, D. R., & Jimenez, J. L. (2008). Development and Characterization of a Fast-Stepping/Scanning Thermodenuder for Chemically-Resolved Aerosol Volatility Measurements. *Aerosol Science and Technology*, *42*(5), 395–407. https://doi.org/10.1080/02786820802104981

Huffman, J. A., Docherty, K. S., Mohr, C., Cubison, M. J., Ulbrich, I. M., Ziemann, P. J., et al. (2009). Chemically-resolved volatility measurements of organic aerosol from different sources. *Environmental Science and Technology*, *43*(14), 5351–5357. https://doi.org/10.1021/es803539d

Jennings, S. G., & O'Dowd, C. D. (1990). Volatility of aerosol at Mace Head, on the west coast of Ireland. *Journal of Geophysical Research*, *95*(D9). https://doi.org/10.1029/jd095id09p13937

Jennings, S. G., O'Dowd, C. D., Cooke, W. F., Sheridan, P. J., & Cachier, H. (1994). Volatility of elemental carbon. *Geophysical Research Letters*, *21*(16), 1719–1722. https://doi.org/10.1029/94GL01423

Jung, C. H., Yoon, Y. J., Kang, H. J., Gim, Y., Lee, B. Y., Ström, J., et al. (2018). The seasonal characteristics of cloud condensation nuclei (CCN) in the arctic lower troposphere. *Https://Doi.Org/10.1080/16000889.2018.1513291*, *70*(1), 1–13. https://doi.org/10.1080/16000889.2018.1513291

Karl, M., Leck, C., Gross, A., & Pirjola, L. (2012). A study of new particle formation in the marine boundary layer over the central Arctic Ocean using a flexible multicomponent aerosol dynamic model. *Tellus B: Chemical and Physical Meteorology*, *64*(1). https://doi.org/10.3402/tellusb.v64i0.17158

Karl, M., Leck, C., Coz, E., & Heintzenberg, J. (2013). Marine nanogels as a source of atmospheric nanoparticles in the high Arctic. *Geophysical Research Letters*, *40*(14), 3738–3743. https://doi.org/10.1002/grl.50661

Kecorius, S., Vogl, T., Paasonen, P., Lampilahti, J., Rothenberg, D., Wex, H., et al. (2019). New particle formation and its effect on cloud condensation nuclei abundance in the summer Arctic: a case study in the Fram Strait and Barents Sea. *Atmospheric Chemistry and Physics*, *19*(22), 14339–14364.

https://doi.org/10.5194/acp-19-14339-2019

Keith, C. H., & Arons, A. B. (1954). The Growth of Sea-Salt Particles by Condensation of Atmospheric Water Vapor. *Journal of Meteorology*, *11*(3). https://doi.org/10.1175/1520-0469(1954)011<0173:TGOSSP>2.0.CO;2

Kim, G., Cho, H., Seo, A., Kim, D., Gim, Y., Yong Lee, B., et al. (2015). Comparison of Hygroscopicity, Volatility, and Mixing State of Submicrometer Particles between Cruises over the Arctic Ocean and the Pacific Ocean. *Environmental Science and Technology*, *49*, 51. https://doi.org/10.1021/acs.est.5b01505

Kirpes, R. M., Bondy, A. L., Bonanno, D., Moffet, R. C., Wang, B., Laskin, A., et al. (2018). Secondary sulfate is internally mixed with sea spray aerosol and organic aerosol in the winter Arctic. *Atmospheric Chemistry and Physics*, *18*(6), 3937–3949. https://doi.org/10.5194/acp-18-3937-2018

Kirpes, R. M., Bonanno, D., May, N. W., Fraund, M., Barget, A. J., Moffet, R. C., et al. (2019). Wintertime Arctic Sea Spray Aerosol Composition Controlled by Sea Ice Lead Microbiology. *ACS Central Science*, *5*(11), 1760–1767. https://doi.org/10.1021/acscentsci.9b00541

Kivekäs, N., Carpman, J., Roldin, P., Leppä, J., O'Connor, E., Kristensson, A., & Asmi, E. (2016). Coupling an aerosol box model with one-dimensional flow: a tool for understanding observations of new particle formation events. *Tellus B: Chemical and Physical Meteorology*, *68*(1), 29706. https://doi.org/10.3402/tellusb.v68.29706

Kolesar, K. R., Cellini, J., Peterson, P. K., Jefferson, A., Tuch, T., Birmili, W., et al. (2017). Effect of Prudhoe Bay emissions on atmospheric aerosol growth events observed in Utqiaġvik (Barrow), Alaska. *Atmospheric Environment*, *152*, 146–155. https://doi.org/10.1016/j.atmosenv.2016.12.019

Kreidenweis, S. M., McInnes, L. M., & Brechtel, F. J. (1998). Observations of aerosol volatility and elemental composition at Macquarie Island during the First Aerosol Characterization Experiment (ACE 1). *Journal of Geophysical Research: Atmospheres*, *103*(D13), 16511–16524. https://doi.org/10.1029/98JD00800

Kuang, C., Riipinen, I., Sihto, S.-L., Kulmala, M., McCormick, A. V., & McMurry, P. H. (2010). An improved criterion for new particle formation in diverse atmospheric environments. *Atmospheric Chemistry and Physics*, *10*(17), 8469–8480. https://doi.org/10.5194/acp-10-8469-2010

Kulmala, M., Dal Maso, M., Mäkelä, J. M., Pirjola, L., Väkevä, M., Aalto, P., et al. (2001). On the formation, growth and composition of nucleation mode particles. *Tellus, Series B: Chemical and Physical Meteorology*, *53*(4), 479–490. https://doi.org/10.3402/tellusb.v53i4.16622

Kupiszewski, P., Leck, C., Tjernström, M., Sjogren, S., Sedlar, J., Graus, M., et al. (2013). Vertical profiling of aerosol particles and trace gases over the central Arctic Ocean during summer. *Atmospheric Chemistry and Physics*, *13*(24), 12405–12431. https://doi.org/10.5194/acp-13-12405-2013

Lance, S., Raatikainen, T., Onasch, T. B., Worsnop, D. R., Yu, X. Y., Alexander, M. L., et al. (2013). Aerosol mixing state, hygroscopic growth and cloud activation efficiency during MIRAGE 2006. *Atmospheric Chemistry and Physics*, *13*(9), 5049–5062. https://doi.org/10.5194/acp-13-5049-2013

Law, K. S., & Stohl, A. (2007). Arctic air pollution: Origins and impacts. *Science*. American Association for the Advancement of Science. https://doi.org/10.1126/science.1137695

Lawler, M. J., Saltzman, E. S., Karlsson, L., Zieger, P., Salter, M., Baccarini, A., et al. (2021). New Insights Into the Composition and Origins of Ultrafine Aerosol in the Summertime High Arctic. *Geophysical Research Letters*, *48*(21), e2021GL094395. https://doi.org/10.1029/2021GL094395

Leaitch, W. R., Sharma, S., Huang, L., Toom-Sauntry, D., Chivulescu, A., Macdonald, A. M., et al. (2013). Dimethyl sulfide control of the clean summertime Arctic aerosol and cloud. *Elementa: Science of the Anthropocene*, *1*(0), 000017. https://doi.org/10.12952/journal.elementa.000017

Leaitch, W. R., Korolev, A., Aliabadi, A. A., Burkart, J., Willis, M. D., Abbatt, J. P. D., et al. (2016). Effects of 20-100nm particles on liquid clouds in the clean summertime Arctic. *Atmospheric Chemistry and Physics*, *16*(17), 11107–11124. https://doi.org/10.5194/ACP-16-11107-2016

Leck, C, Gao, Q., Mashayekhy Rad, F., & Nilsson, U. (2013). Atmospheric Chemistry and Physics Size-resolved atmospheric particulate polysaccharides in the high summer Arctic. *Atmospheric Chemistry and Physics*, *13*, 12573–12588. https://doi.org/10.5194/acp-13-12573-2013

Leck, Caroline, & Bigg, E. K. (2010). New Particle Formation of Marine Biological Origin. *Aerosol Science and Technology*, *44*(7), 570–577. https://doi.org/10.1080/02786826.2010.481222

Liao, J., Huey, L. G., Tanner, D. J., Flocke, F. M., Orlando, J. J., Neuman, J. A., et al. (2012). Observations of inorganic bromine (HOBr, BrO, and Br2) speciation at Barrow, Alaska, in spring 2009. *Journal of Geophysical Research: Atmospheres*, *117*(D14). https://doi.org/10.1029/2011JD016641@10.1002/(ISSN)2169-8996.OASIS1

Liu, S., Aiken, A. C., Gorkowski, K., Dubey, M. K., Cappa, C. D., Williams, L. R., et al. (2015). Enhanced light absorption by mixed source black and brown carbon particles in UK winter. *Nature Communications*. https://doi.org/10.1038/ncomms9435

Malm, W. C., & Kreidenweis, S. M. (1997). The effects of models of aerosol hygroscopicity on the apportionment of extinction. *Atmospheric Environment*, *31*(13), 1965–1976. https://doi.org/10.1016/S1352-2310(96)00355-X

Martin, M., Chang, R. Y. W., Sierau, B., Sjogren, S., Swietlicki, E., Abbatt, J. P. D., et al. (2011). Cloud condensation nuclei closure study on summer arctic aerosol. *Atmospheric Chemistry and Physics*, *11*(22), 11335–11350. https://doi.org/10.5194/ACP-11-11335-2011

Mauldin, R. L., Frost, G. J., Chen, G., Tanner, D. J., Prevot, A. S. H., Davis, D. D., & Eisele, F. L. (1998). OH measurements during the First Aerosol Characterization Experiment (ACE 1): Observations and model comparisons. *Journal of Geophysical Research: Atmospheres*, *103*(D13), 16713–16729. https://doi.org/10.1029/98JD00882

Mauritsen, T., Sedlar, J., TjernstrÃm, M., Leck, C., Martin, M., Shupe, M., et al. (2011). An Arctic CCN-limited cloud-aerosol regime. *Atmospheric Chemistry and Physics*, *11*(1), 165–173. https://doi.org/10.5194/ACP-11-165-2011

May, N. W., Quinn, P. K., McNamara, S. M., & Pratt, K. A. (2016). Multiyear study of the dependence of sea salt aerosol on wind speed and sea ice conditions in the coastal Arctic. *Journal of Geophysical Research: Atmospheres*, *121*(15), 9208–9219. https://doi.org/10.1002/2016JD025273

Mendes, L., Eleftheriadis, K., & Biskos, G. (2016). Performance comparison of two thermodenuders in Volatility Tandem DMA measurements. *Journal of Aerosol Science*, *92*, 38–52. https://doi.org/https://doi.org/10.1016/j.jaerosci.2015.10.002

Modini, R. L., Johnson, G. R., He, C., & Ristovski, Z. D. (2010). Observation of the suppression of water uptake by marine particles. *Atmospheric Research*, *98*(2–4), 219–228. https://doi.org/10.1016/J.ATMOSRES.2010.03.025

Moore, R. H., Bahreini, R., Brock, C. A., Froyd, K. D., Cozic, J., Holloway, J. S., et al. (2011). Hygroscopicity and composition of Alaskan Arctic CCN during April 2008. *Atmospheric Chemistry and Physics*, *11*(22), 11807–11825. https://doi.org/10.5194/ACP-11-11807-2011

NCAR. (2012). Location information and pictures of the OASIS Barrow field intensive Spring 2009. Retrieved February 3, 2021, from https://data.eol.ucar.edu/dataset/106.366

Nguyen, Q. T., Glasius, M., Sørensen, L. L., Jensen, B., Skov, H., Birmili, W., et al. (2016). Seasonal variation of atmospheric particle number concentrations, new particle formation and atmospheric oxidation capacity at the high Arctic site Villum Research Station, Station Nord. *Atmospheric Chemistry and Physics*, *16*, 11319–11336. https://doi.org/10.5194/acp-16-11319-2016

Nilsson, E. D., Rannik, Ü., Swietlicki, E., Leck, C., Aalto, P. P., Zhou, J., & Norman, M. (2001). Turbulent aerosol fluxes over the Arctic Ocean: 2. Wind-driven sources from the sea. *Journal of Geophysical Research: Atmospheres*, *106*(D23), 32139–32154. https://doi.org/10.1029/2000JD900747

Nyeki, S., Coulson, G., Colbeck, I., Eleftheriadis, K., Baltensperger, U., & Beine, H. J. (2005). Overview of aerosol microphysics at Arctic sunrise: measurements during the NICE renoxification study. *Tellus B*, *57*(1), 40–50. https://doi.org/10.1111/j.1600-0889.2005.00122.x

O'Dowd, C. D., Facchini, M. C., Cavalli, F., Ceburnis, D., Mircea, M., Decesari, S., et al. (2004). Biogenically driven organic contribution to marine aerosol. *Nature*, *431*(7009), 676–680. https://doi.org/10.1038/nature02959

Ovadnevaite, J., Ceburnis, D., Martucci, G., Bialek, J., Monahan, C., Rinaldi, M., et al. (2011). Primary marine organic aerosol: A dichotomy of low hygroscopicity and high CCN activity. *Geophysical Research Letters*, *38*(21). https://doi.org/https://doi.org/10.1029/2011GL048869

Oxford, C. R., Dang, A. J., Rapp, C. M., & Williams, B. J. (2020). Interpretation of Volatility Tandem Differential Mobility analyzer (V-TDMA) data for accurate vapor pressure and enthalpy measurement: Operational considerations, multiple chargin, and introduction to new analyisis program (TAO). *Aerosol Science and Technology*, *54*(4), 410–425. Retrieved from https://doi.org/10.1080/02786826.2019.1709617

Park, S. H., Rogak, S. N., & Grieshop, A. P. (2013). A Two-Dimensional Laminar Flow Model for Thermodenuders Applied to Vapor Pressure Measurements. *Aerosol Science and Technology*, *47*(3), 283–293.

Patterson, E. M., Marshall, B. T., & Rahn, K. A. (1967). Radiative properties of the arctic aerosol. *Atmospheric Environment*, *16*(12), 2967–2977. https://doi.org/10.1016/0004-6981(82)90048-8

Petters, M. D., & Kreidenweis, S. M. (2007). A single parameter representation of hygroscopic growth and cloud condensation nucleus activity. *Atmospheric Chemistry and Physics*, *7*, 1961–1971. Retrieved from www.atmos-chem-phys.net/7/1961/2007/

Polissar, A. V., Hopke, P. K., & Harris, J. M. (2001). Source regions for atmospheric aerosol measured at Barrow, Alaska. *Environmental Science and Technology*, *35*(21), 4214–4226. https://doi.org/10.1021/es0107529

Prather, K. A., Bertram, T. H., Grassian, V. H., Deane, G. B., Stokes, M. D., DeMott, P. J., et al. (2013). Bringing the ocean into the laboratory to probe the chemical complexity of sea spray aerosol. *Proceedings of the National Academy of Sciences of the United States of America*, *110*(19), 7550–7555. https://doi.org/10.1073/pnas.1300262110

Quinn, P. K., Miller, T. L., Bates, T. S., Ogren, J. A., Andrews, E., & Shaw, G. E. (2002). A 3-year record of simultaneously measured aerosol chemical and optical properties at Barrow, Alaska. *Journal of Geophysical Research D: Atmospheres*, *107*(11), AAC 8-1. https://doi.org/10.1029/2001jd001248

Quinn, P. K., Shaw, G., Andrews, E., & Dutton, E. G. (2007). Arctic haze: current trends and knowledge gaps. *Tellus B: Chemical and Physical Meteorology*. https://doi.org/10.1111/j.1600-0889.2006.00236.x

Quinn, P. K., Bates, T. S., Schulz, K., & Shaw, G. E. (2009). Decadal trends in aerosol chemical composition at Barrow, Alaska: 1976-2008. *Atmospheric Chemistry and Physics*, *9*, 8883–8888. Retrieved from www.atmos-chem-phys.net/9/8883/2009/

Quinn, P. K., Bates, T. S., Coffman, D. J., Upchurch, L., Johnson, J. E., Moore, R., et al. (2019). Seasonal Variations in Western North Atlantic Remote Marine Aerosol Properties. *Journal of Geophysical Research: Atmospheres*, *124*(24), 14240–14261. https://doi.org/10.1029/2019JD031740

Rahn, K. A. (1981). Relative importances of North America and Eurasia as sources of arctic aerosol. *Atmospheric Environment (1967)*, *15*(8), 1447–1455. https://doi.org/10.1016/0004-6981(81)90351-6

Randelhoff, A., Lacour, L., Marec, C., Leymarie, E., Lagunas, J., Xing, X., et al. (2020). Arctic mid-winter phytoplankton growth revealed by autonomous profilers. *Science Advances*, *6*(39), eabc2678. https://doi.org/10.1126/SCIADV.ABC2678

Rolph, G., Stein, A., & Stunder, B. (2017). Real-time Environmental Applications and Display sYstem: READY. *Environmental Modelling & Software*, *95*(1364–8152), 210–228. Retrieved from https://doi.org/10.1016/j.envsoft.2017.06.025

Sakurai, H., Fink, M. A., McMurry, P. H., Mauldin, L., Moore, K. F., Smith, J. N., & Eisele, F. L. (2005). Hygroscopicity and volatility of 4–10 nm particles during summertime atmospheric nucleation events in urban Atlanta. *Journal of Geophysical Research*, *110*(D22), D22S04. https://doi.org/10.1029/2005JD005918

Saleh, R., Shihadeh, A., & Khlystov, A. (2011). On transport phenomena and equilibration time scales in thermodenuders. *Atmospheric Measurement Techniques*, *4*, 571–581. Retrieved from https://doi.org/10.5194/amt-4-571-2011

Shantz, N. C., Gultepe, I., Andrews, E., Zelenyuk, A., Earle, M. E., Macdonald, A. M., et al. (2014). Optical, physical, and chemical properties of springtime aerosol over Barrow Alaska in 2008. *International Journal of Climatology*, *34*(10). https://doi.org/10.1002/joc.3898

Shaw, G. E. (1986). Cloud condensation nuclei associated with arctic haze. *Atmospheric Environment (1967)*, *20*(7), 1453–1456. https://doi.org/10.1016/0004-6981(86)90017-X

Shaw, P. M., Russell, L. M., Jefferson, A., & Quinn, P. K. (2010). Arctic organic aerosol measurements show particles from mixed combustion in spring haze and from frost flowers in winter. *Geophysical Research Letters*, *37*(10), n/a-n/a. https://doi.org/10.1029/2010GL042831

Sjogren, S., Gysel, M., Weingartner, E., Baltensperger, U., Cubison, M. J., Coe, H., et al. (2007). Hygroscopic growth and water uptake kinetics of two-phase aerosol particles consisting of ammonium sulfate, adipic and humic acid mixtures. *Journal of Aerosol Science*, *38*(2), 157–171. https://doi.org/10.1016/j.jaerosci.2006.11.005

Stein, A. F., Draxler, R. R., Rolph, G. D., Stunder, B. J. B., Cohen, M. D., & Ngan, F. (2015). NOAA's HYSPLIT Atmospheric Transport and Dispersion Modeling System. *Bulletin of the American Meteorological Society*, *96*, 2059–2077. Retrieved from https://doi.org/10.1175/BAMS-D-14-00110.1

Stokes, R. H., & Robinson, R. A. (1966). Interactions in aqueous nonelectrolyte solutions. I. Solute-solvent equilibria. *Journal of Physical Chemistry*, *70*(7), 2126–2131. https://doi.org/10.1021/j100879a010

Ström, J., Umegård, J., Tørseth, K., Tunved, P., Hansson, H. C., Holmén, K., et al. (2003). One year of particle size distribution and aerosol chemical composition measurements at the Zeppelin Station, Svalbard, March 2000-March 2001. *Physics and Chemistry of the Earth*, *28*(28–32), 1181–1190. https://doi.org/10.1016/j.pce.2003.08.058

Tanner, D. J., Jefferson, A., & Eisele, F. L. (1997). Selected ion chemical ionization mass spectrometric measurement of OH. *Journal of Geophysical Research Atmospheres*, *102*(5), 6415–6425. https://doi.org/10.1029/96jd03919

Thompson, C. R., Shepson, P. B., Liao, J., Huey, L. G., Apel, E. C., Cantrell, C. A., et al. (2015). Interactions of bromine, chlorine, and iodine photochemistry during ozone depletions in Barrow, Alaska. *Atmospheric Chemistry and Physics*, *15*, 9651–9679. https://doi.org/10.5194/acp-15-9651-2015

Tomasi, C., Lupi, A., Mazzola, M., Stone, R. S., Dutton, E. G., Herber, A., et al. (2012). An update on polar aerosol optical properties using POLAR-AOD and other measurements performed during the International Polar Year. *Atmospheric Environment*, *52*, 29–47. https://doi.org/10.1016/j.atmosenv.2012.02.055

Tremblay, S., Picard, J.-C., Bachelder, J. O., Lutsch, E., Strong, K., Fogal, P., et al. (2019). Characterization of aerosol growth events over Ellesmere Island during the summers of 2015 and 2016. *Atmos. Chem. Phys*, *19*, 5589–5604. https://doi.org/10.5194/acp-19-5589-2019

Tunved, P., Ström, J., & Krejci, R. (2013). Arctic aerosol life cycle: linking aerosol size distributions observed between 2000 and 2010 with air mass transport and precipitation at Zeppelin station, Ny-Ålesund, Svalbard. *Atmospheric Chemistry and Physics*, *13*(7), 3643–3660. https://doi.org/10.5194/acp-13-3643-2013

Verdugo, P. (2012). Marine Microgels. *Annual Review of Marine Science*, *4*(1), 375–400. https://doi.org/10.1146/annurev-marine-120709-142759

Verdugo, P., & Santschi, P. H. (2010). Polymer dynamics of DOC networks and gel formation in seawater. *Deep Sea Research Part II: Topical Studies in Oceanography*, *57*(16). https://doi.org/10.1016/j.dsr2.2010.03.002

Villani, P., Picard, D., Marchand, N., & Laj, P. (2007). Design and validation of a 6-volatility tandem differential mobility analyzer (VTDMA). *Aerosol Science and Technology*, *41*(10), 898–906. https://doi.org/10.1080/02786820701534593

Virkkula, A., Van Dingenen, R., Raes, F., & Hjorth, J. (1999). Hygroscopic properties of aerosol formed by oxidation of limonene, α-pinene, and β-pinene. *Journal of Geophysical Research Atmospheres*, *104*(D3), 3569–3579. https://doi.org/10.1029/1998JD100017

Wehner, B., Philippin, S., & Wiedensohler, A. (2002). Design and calibration of a thermodenuder with an improved heating unit to measure the size-dependent volatile fraction of aerosol particles. *Journal of Aerosol Science*, *33*(7), 1087–1093. https://doi.org/10.1016/S0021-8502(02)00056-3

Weingartner, E., Gysel, M., & Baltensperger, U. (2001). Hygroscopicity of Aerosol Particles at Low Temperatures. 1. New Low-Temperature H-TDMA Instrument: Setup and First Applications. *Environmental Science and Technology*, *36*(1), 55–62. https://doi.org/10.1021/ES010054O

Weingartner, E., Baltensperger, U., & Burtscher, H. (1995). Growth and Structural Change of Combustion Aerosols at High Relative Humidity. *Environmental Science and Technology*, *29*(12), 2982–2986. https://doi.org/10.1021/es00012a014

Wiedensohler, A. (1988). An approximation of the bipolar charge distribution for particles in the

submicron size range. *Journal of Aerosol Science*, *19*(3), 387–389. https://doi.org/10.1016/0021-8502(88)90278-9

Wiedensohler, A., Covert, D. S., Swietlecki, E., Aalto, P., Heintzenberg, J., & Leck, C. (1996). Occurrence of an ultrafine particle mode less than 20 nm in diameter in the marine boundary layer during Arctic summer and autumn. *Tellus B*, *48*(2), 213–222. https://doi.org/10.1034/j.1600-0889.1996.t01-1-00006.x

Willis, M. D., Burkart, J., Thomas, J. L., Köllner, F., Schneider, J., Bozem, H., et al. (2016). Growth of nucleation mode particles in the summertime Arctic: a case study. *Atmospheric Chemistry and Physics*, *16*, 7663–7679. https://doi.org/10.5194/acp-16-7663-2016

Zábori, J., Rastak, N., Yoon, Y. J., Riipinen, I., & Ström, J. (2015). Size-resolved cloud condensation nuclei concentration measurements in the Arctic: two case studies from the summer of 2008. *Atmospheric Chemistry and Physics*, *15*, 13803–13817. https://doi.org/10.5194/acp-15-13803-2015

Zheng, G., Wang, Y., Wood, R., Jensen, M. P., Kuang, C., McCoy, I. L., et al. (2021). New particle formation in the remote marine boundary layer. *Nature Communications*, *12*(1). https://doi.org/10.1038/s41467-020-20773-1

Zieger, P., Väisänen, O., Corbin, J. C., Partridge, D. G., Bastelberger, S., Mousavi-Fard, M., et al. (2017). Revising the hygroscopicity of inorganic sea salt particles. *Nature Communications*, *8*. https://doi.org/10.1038/ncomms15883

Ziemba, L. D., Dibb, J. E., Griffin, R. J., Huey, L. G., & Beckman, P. (2010). Observations of particle growth at a remote, Arctic site. *Atmospheric Environment*, *44*(13), 1649–1657. https://doi.org/10.1016/j.atmosenv.2010.01.032